

In-depth analysis of the genomic landscape of 86 metastatic neuroendocrine neoplasms reveals subtype-heterogeneity and potential therapeutic targets

Bianca Mostert (✉ b.mostert@erasmusmc.nl)

Erasmus MC Cancer Institute

Job van Riet

Erasmus University Medical Center <https://orcid.org/0000-0001-7767-7923>

Harmen van de Werken

Erasmus MC <https://orcid.org/0000-0002-9794-1477>

Edwin Cuppen

Hartwig Medical Foundation

Ferry Eskens

Erasmus MC Cancer Institute

Margot Tesselaar

University of Amsterdam

Linde Veenendaal

University of Amsterdam

Heinz-Josef Klümpen

Amsterdam University Medical Centers

Marcus Dercksen

Maxima Medisch Centrum

Gerlof Valk

University Medical Center Utrecht

Martijn Lolkema

Erasmus University Medical Center <https://orcid.org/0000-0003-0466-2928>

Stefan Sleijfer

Erasmus MC

Article

Keywords: neuroendocrine, neoplasm, neuroendocrine tumors, whole-genome sequencing, CPCT02, metastasis, therapy targets

Posted Date: August 25th, 2020

DOI: <https://doi.org/10.21203/rs.3.rs-50333/v1>

License:  This work is licensed under a Creative Commons Attribution 4.0 International License.

[Read Full License](#)

Version of Record: A version of this preprint was published at Nature Communications on July 29th, 2021. See the published version at <https://doi.org/10.1038/s41467-021-24812-3>.

In-depth analysis of the genomic landscape of 86 metastatic neuroendocrine neoplasms reveals subtype-heterogeneity and potential therapeutic targets

Job van Riet^{1,2,3*}, Harmen J. G. van de Werken^{1-2*}, Edwin Cuppen^{4,10}, Ferry A. L. M. Eskens³, Margot Tesselaar⁵, Linde M. van Veenendaal⁵, Heinz-Josef Klümpen⁶, Marcus W. Dercksen⁷, Gerlof D. Valk⁸, Martijn P. Lolkema^{3,9}, Stefan Sleijfer^{3,9}, Bianca Mostert^{3†}

1. Cancer Computational Biology Center, Erasmus MC Cancer Institute, University Medical Center, Wytemaweg 80, 3015 CN, Rotterdam, the Netherlands.
2. Department of Urology, Erasmus MC Cancer Institute, University Medical Center, Wytemaweg 80, 3015 CN, Rotterdam, the Netherlands.
3. Department of Medical Oncology, Erasmus MC Cancer Institute, Rotterdam, the Netherlands.
4. Center for Molecular Medicine and Onco Institute, University Medical Center Utrecht, Heidelberglaan 100, 3584 CX, Utrecht, the Netherlands.
5. Department of Medical Oncology, Cancer Institute, University of Amsterdam, The Netherlands.
6. Department of Medical Oncology, Amsterdam University Medical Centers, Cancer Center Amsterdam, Amsterdam, The Netherlands.
7. Department of Internal Medicine, Maxima Medisch Centrum, Veldhoven, The Netherlands.
8. Department of Endocrine Oncology, University Medical Center Utrecht, Utrecht, The Netherlands.
9. Center for Personalized Cancer Treatment, Rotterdam, the Netherlands.
10. Hartwig Medical Foundation, Amsterdam, the Netherlands.

* These authors contributed equally.

† Corresponding author.

Address for correspondence:

Postbus 2040

3000 CA Rotterdam

b.mostert@erasmusmc.nl

Journal information:

Journal: Nature Communications

Number of text pages: 35

Number of tables: 1 supplementary table.

Number of figures: 5 figures, 10 supplementary figures.

Requirements: main text (excl. abstract, online Methods, refs and fig legends) is 2,000-4,000 words; abstract 100 words; max 8 figures/tables; Introduction (without heading), followed by results (incl subheadings), discussion, online methods (incl subheadings)

Keywords: neuroendocrine; neoplasm; neuroendocrine tumors; whole-genome sequencing; CPCT02; metastasis; therapy targets

36 **Abstract**

37 Metastatic neuroendocrine neoplasms (mNEN) form clinically and genetically
38 heterogeneous malignancies, characterized by distinct prognoses based upon primary
39 tumor localization, functionality, grade, proliferation index and diverse outcomes to
40 treatment. Here, we report the mutational landscape of 86 whole-genome sequenced
41 mNEN. This landscape revealed distinct genomic subpopulations of mNEN based on primary
42 localization and differentiation grade; we observed relatively high tumor mutational
43 burdens (TMB) in neuroendocrine carcinoma (5.45 somatic mutations per megabase) with
44 *TP53*, *KRAS*, *RB1*, *MYC* and *APC* as major drivers versus an overall low TMB in
45 neuroendocrine tumors (1.08). Furthermore, we observed distinct drivers which were
46 enriched with somatic aberrations in pancreatic (*MEN1*, *ATRX*, *DAXX*, *PCNT* and *SETD2*) and
47 midgut-derived neuroendocrine tumors (*CDKN1B*). Finally, 49% of mNEN patients revealed
48 extensions of their treatment-repertoire based upon actionable (and responsive) somatic
49 aberrations; potentially directing improvements in mNEN treatment strategies.

50 **Introduction**

51 Neuroendocrine neoplasms (NEN) is a heterogeneous and uncommon tumor type. It can
52 arise from any of the neuroendocrine cells distributed widely throughout the body.
53 Clinically, a distinction is made between the poorly differentiated neuroendocrine
54 carcinomas (NEC) and the better differentiated neuroendocrine tumors (NET)¹, the latter
55 are further subdivided based on their primary site in pancreas (pNET), gastro-intestinal tract
56 or lung NET. Further distinctions are made based upon grade (as assessed by Ki-67 or MIB-1
57 staining as a measure of proliferation index), differentiation, histology (small-cell vs. large-
58 cell) and functionality (the presence or absence of hormone secretion resulting in typical
59 clinical syndromes dependent upon the predominant hormone that is secreted). Tumor
60 grade and differentiation are associated with prognosis, and all the aforementioned factors
61 affect the choice of treatment. However, also in small subgroups of NEN, such as well-
62 differentiated low-proliferating pNET, marked clinical and genetic heterogeneity occur, as
63 well as, vastly different responses to treatment. Thus, the parameters by which NEN are
64 currently classified do not sufficiently separate patients and tumors according to prognosis
65 and response to therapy. Nonetheless, certain anti-tumor therapies (i.e., sunitinib and
66 everolimus) have been registered for distinct NEN-subtypes. Hence, there is a high unmet
67 need to better classify and understand these diverse tumors, ultimately leading to more
68 tumor- or patient-tailored therapeutic strategies.

69

70 Thus far, limited whole genome sequencing data are available for NEN, probably reflecting
71 the rarity of this disease. Currently, pNET have been characterized most extensively; 81
72 primary tumors were subjected to whole genome sequencing as part of the PCAWG project²
73 and another 104 primary pNET were described by Scarpa et al.³. Additionally, smaller series
74 have been published containing lung and gastrointestinal NET.^{4,5} These studies have shown
75 that NET have a relatively stable genome and only few driver mutations. However, these
76 studies were all performed on primary tumor specimens, whilst a patient generally dies
77 from the consequences of metastatic disease. Additionally, we know from other tumor
78 types that marked heterogeneity can occur between primary and metastatic tumor cells⁶⁻⁹,
79 due to inherent genomic instability and/or the influence of targeted or cytotoxic treatment
80 on the tumor genome. These discrepancies should be taken into account when assessing a
81 patient's prognosis and possible treatment options, and can be better understood through

82 thorough genomic characterization of metastases. To date, analysis of metastatic NET is
83 limited to two studies describing series of five patients with NET originating in the pancreas
84 and the small intestine (or midgut), respectively.^{10,11} These studies have shown focal
85 amplification of *MYCN* concomitant with loss of *APC* and *TP53* in one sample as important
86 metastatic genetic aberrations. For NECs, only two series of whole genome sequencing of
87 the primary tumors of 1) five cervical and 2) 12 genitourinary NECs have been published.^{12,13}

88

89 Whole genome sequencing was performed on 86 NEN metastases (mNEN), one per distinct
90 patient, which were biopsied as part of the CPCT-02 study.¹⁴ We report here on the
91 presence of genomic alterations, mutational and rearrangement signatures for the whole
92 mNEN cohort and reveal genomic characteristics and alterations distinguishing mNEC from
93 mNET. Furthermore, we make a genomic distinction between pancreas- and midgut-derived
94 mNET. Additionally, we investigated the presence of actionable genetic alteration within
95 mNEN patients, which might render them eligible for off-label or experimental systemic
96 treatments to extend therapy options.

97 **Results**

98 **Overview of included patients within the CPCT-02 mNEN cohort.**

99 A total of 109 patients, originally classified as having a neuroendocrine neoplasm, were
100 included in the CPCT-02 study and had a metastatic biopsy taken in parallel with a blood
101 control (**Figure 1**). Five patients were excluded because of missing or withdrawn informed
102 consent, and another five had non-evaluable biopsies due to low (<20%) tumor cell
103 percentage or low DNA yield. Thirteen biopsies were excluded because of incomplete
104 clinical records, misclassifications of the tumor (based on additional checks of the medical
105 records), or were duplicate biopsies from the same patient. An overview of the mNEN
106 patient inclusion per participating Dutch center ($n = 13$) can be found in **Supplementary**
107 **Figure 1**.

108

109 The metastatic tumor biopsies and corresponding peripheral blood controls from the
110 remaining 86 distinct patients were whole genome sequenced using paired-end protocols,
111 to a median mean read coverage of 107x (Q(uartile)₁-Q₃: 99x-115x) and 38x (Q₁-Q₃: 35-42x),

112 respectively to a median *in silico* estimated tumor cell purity of 0.7 (Q₁-Q₃: 0.5-0.81)
113 (Supplementary figure 2a-b).

114

115 The mNEN cohort is represented by 37 females and 49 males of a median age of 62 (Q₁-Q₃:
116 57-68) and 61 (Q₁-Q₃: 56-68), at time of biopsy respectively. In total, 70 NET and 16 NEC
117 were included. The primary tumor location in the midgut was most common (*n* = 42, 49%),
118 followed by pancreas (*n* = 24, 28%) and unknown (*n* = 12, 14%) (Figure 1). Most of the tumor
119 biopsies were taken from liver metastases, and a minority from relapses at the primary site
120 (Supplementary figure 2c-d).

121

122 **The mutational landscape of metastatic neuro-endocrine neoplasms reveals differences related to primary**
123 **localization and degree of differentiation.**

124 The overall mutational landscape of mNEN (*n* = 86; Figure 2) reveals two strikingly distinct
125 genomic populations of neuroendocrine neoplasms, i.e. the mNEC and mNET populations.
126 The mNEC (*n* = 16) reveals diploid to triploid genomes and a median tumor mutational
127 burden (TMB) of 5.45 somatic mutations per Mb (Q₁-Q₃: 3.8 - 8.85), which is in the mid-
128 range of TMB known for human primary cancers¹⁵. However, the mNET (*n* = 70) are
129 hallmarked by a relatively stable diploid tumor genome with only few, but specific,
130 chromosomal arm aberrations and harbors the lowest overall TMB of only 1.08 (Q₁-Q₃: 0.78
131 - 1.54) of all metastatic cohorts within the CPCT-02 study.¹⁴

132

133 The somatically-acquired and whole-genomic mutational landscape of mNEC (*n* = 16)
134 revealed a median of 13996 single-nucleotide variants (SNVs; Q₁-Q₃: 9465 - 22830), 1755
135 small insertions and deletions (InDels; Q₁-Q₃: 751 - 2244), 114 multiple-nucleotide variants
136 (MNVs; Q₁-Q₃: 49 - 198), 150 structural variants (SVs; Q₁-Q₃: 82 - 264) and an overall diploid
137 to triploid genome (Q₁-Q₃: 1.9 - 3.1; Supplementary figure 3). Concordant with the lower
138 TMB of the mNET (*n* = 70), the mNET revealed a median of 2822 SNVs (Q₁-Q₃: 1982 - 3892),
139 254 InDels (Q₁-Q₃: 185 - 329), 18 MNVs (Q₁-Q₃: 12 - 27), 17 Structural Variants (SVs; Q₁-Q₃: 7
140 - 56) and an overall diploid genome (Q₁-Q₃: 1.9 - 2.1). The discrepancy in mutational load
141 between mNEC and mNET also held true when inspecting only the coding regions, in which
142 mNEC revealed a higher number of SNVs, InDels, MNV compared to mNET (Supplementary

143 **figure 3a**). Similarly, mNEC displayed elevated numbers of all SV classes (translocations,
144 deletions, tandem duplications, insertions and inversions; **Supplementary figure 3d**).

145

146 The majority of somatic coding mutations for all mNEC and all mNET ($n = 2730$ and 3127 ;
147 SNV, InDel and MNV) were found to be predicted missense variants (59% in mNEC vs. 55%
148 in mNET), followed by synonymous variants (21% vs. 22%). The number of genes harboring
149 somatic mutations within their coding regions differed between mNEC and mNET. Over the
150 entire mNEC cohort ($n = 16$), 2841 distinct mutant genes were observed, versus 3134
151 distinct genes within the entire mNET cohort ($n = 70$). Per sample, a median of 149 (Q_1 - Q_3 :
152 127 - 270) versus 37 (median; Q_1 - Q_3 : 26 - 50) genes harboring mutations within coding
153 regions were observed for mNEC and mNET samples respectively; revealing that mNEC
154 harbor greater numbers of mutant genes compared to mNET.

155

156 The median genome-wide ratio of transitions (T_i ; $A \leftrightarrow G$ or $T \leftrightarrow C$) to transversions (T_v ;
157 $C \leftrightarrow A$, $C \leftrightarrow G$, $T \leftrightarrow A$ or $T \leftrightarrow G$) within mNEC was found to be 0.78 $T_i \setminus T_v$ (Q_1 - Q_3 : 0.72 - 1.02)
158 vs. 1.52 $T_i \setminus T_v$ (Q_1 - Q_3 : 1.12 - 2.20) in the coding regions. For mNET the median genome-wide
159 and coding $T_i \setminus T_v$ were found to be 1.11 (Q_1 - Q_3 : 0.99 - 1.32) and 1.42 (Q_1 - Q_3 : 1 - 1.96),
160 respectively (**Supplementary figure 3f**).

161

162 High TMB (≥ 10) are often associated with DNA repair deficiency and/or tumors with
163 sensitivity for immune therapy, e.g. checkpoint inhibitors. Four mNEC samples, all from
164 unknown origin, and a single pancreatic mNET showed this high-TMB genotype (**Figure 2a**).
165 One mNET displayed signs of *BRCA2*-associated homologous recombination deficiency
166 (HRD), as determined using the CHORD classifier which is mainly based on deletions with
167 flanking microhomology and 1-100kb structural duplications (**Figure 2j; supplementary**
168 **figure 4**). Further inspection revealed that this mNET harbored a somatic frameshift
169 mutation within *RAD51C*, a known HRD-associated gene.¹⁶

170 **Regional hypermutation (kataegis).**

171 Regional hypermutation (kataegis) was detected in six mNEC; **Figure 2i; supplementary**
172 **Figure 5**). Canonically, kataegis is associated with *APOBEC*-activity and indeed, four out of
173 five (80%) of these kataegis events predominantly showed the canonical TpCpW context

174 associated with *APOBEC* alterations.¹⁷ Additionally, in the samples with kataegis ($n = 5$), the
175 absolute contribution of *APOBEC* SBS signatures (2 & 13) was significantly higher (median 45
176 vs. 533, $p < 0.01$, Wilcoxon rank-sum test) compared to mNEN without kataegis ($n = 81$).

177 **Chromothripsis**

178 Multiple distinct mNEN (four mNEC and two mNET; 7%) revealed presence of
179 chromothripsis, a catastrophic phenomenon of the shattering and interchromosomal
180 recombination of one or more chromosomes (**Figure 2h; Supplementary figure 6**).
181 Strikingly, four of the six observed chromothripsis events from distinct mNEN (two mNEC
182 and two mNET) involved the same chromosome, namely chromosome 12. Within these four
183 mNEN, we observed possible evidence for extrachromosomal DNA due to copy-number
184 oscillations between one low ($CN \leq 4$) and one very high ($CN \geq 10$) states, consistent with the
185 presence of double minutes.^{18–20} Several known oncogenes lie within these regions on
186 chromosome 12, including *MDM2* and possibly *CCND2*, and could be related to a
187 phenomena which generates extrachromosomal DNA which has been described previously
188 in primary tumors within the PCAWG cohort.¹⁸

189 **Catalog of the cohort-wide mutational signatures provide biological insights into treatment effect.**

190 Different mutational processes, such as exposure to exogenous or endogenous mutagens
191 and defective DNA repair mechanisms generate unique combinations of mutational
192 trinucleotide contexts which are reflected in mutational signatures.^{21,22} To determine these
193 mutational signatures within mNEN, we performed *de novo* mutational signature analysis
194 and determined the contribution of previously described single base substitution (SBS)
195 mutational signatures (COSMIC v3). The *de novo* mutational signature assessment revealed
196 seven signatures, denoted as Sig. A to Sig. G, (**supplementary figure 7d**) which all strongly
197 correlated to previously known mutational signatures (**supplementary figure 7a-c**). In
198 particular, we observed samples with large relative contributions (>20%) of *de novo*
199 signatures similar to the known signatures associated with aging (SBS1 & 5; Sig A and D),
200 *APOBEC* activity (SBS2 & 13; Sig B.), tobacco smoking (SBS4; Sig F.), alkylating agents
201 exposure (SBS11; Sig E.), 5-Fluorouracil exposure (SBS17a-b; Sig. C.) and *MUTYH* mutations
202 (SBS36; Sig. G.).

203

204 Overall, the mutational signature profiles do not differ greatly within the mNEN cohort.
205 SBS5 ($n = 48$; putative clock-like), SBS8 ($n = 45$; Unknown), SBS40 ($n = 22$; Unknown), SBS3 (n
206 $= 16$; HRD-like), SBS1 ($n = 10$; clock-like), SBS39 ($n = 7$; Unknown) and SBS9 ($n = 5$;
207 polymerase η (*POLH*) activity) were classified as dominant signatures (i.e., contributed at
208 least 10% of total contribution within ≥ 5 mNEN; **Figure 2e**).

209

210 Two included mNEC of unknown primary localization are characterized by high-TMB (≥ 10)
211 and SBS4, which is associated with smoking; likely due to tobacco mutagens. This could
212 reflect that these metastases could be primary lung NEC, as a relation between mNEC on
213 non-pulmonary origin and smoking is not known. However, as no somatic coding mutations
214 in canonical lung cancer-associated genes were observed and the clinicopathological data of
215 these patients did not point to any different primary tumor other than a NEC, it seems
216 unlikely that these could be primary non-small cell lung cancers.

217

218 Strikingly, the only high-TMB (pancreatic) NET was strongly characterized by SBS11 which
219 exhibits a mutational pattern resembling that of alkylating agents, with a strong enrichment
220 for C/T (G>A) transitions. Previously, an association between treatment with the alkylating
221 agent temozolomide and SBS11 mutations has been found.^{21,23} This same patient showed
222 the highest tumor mutational burden with a TMB of 21.4 (median TMB of NET: 1.1) and was
223 treated with a combination of 5-fluorouracil and streptozocin before undergoing a biopsy
224 for the CPCT-02 study. Streptozocin is capable of DNA alkylation and inhibition of DNA
225 synthesis, and its mechanism of action closely resembles that of temozolomide.

226

227 One mNET was strongly characterized by SBS36, associated with base excision repair (BER)
228 deficiency due to *MUTYH* alterations, C>A mutations and previously also seen in pancreatic
229 NET.²³⁻²⁵ Strikingly, this tumor did not harbor specific somatic alterations within *MUTYH* but
230 possessed a heterozygous germline pathogenic missense mutation within *MUTYH*
231 (c.527A>G / p.Tyr176Cys; rs34612342) coupled with a complete loss of a single chromosome
232 1, resulting in subsequent loss-of-heterozygosity.

233 Driver catalog of mNEN

234 Utilizing unbiased driver gene discovery by GISTIC2 and dN/dS on the entire mNEN cohort
235 and separately on all mNET and mNEC samples, we detected seventeen focal deletion peaks
236 and two focal copy-number amplifications peaks throughout the genome ($q \leq 0.1$) and nine
237 genes enriched with non-synonymous mutations ($q \leq 0.1$; **figure 3 and supplementary**
238 **figure 8**). Within these focal peaks, several oncogenes and tumor suppressors were present
239 which could be the potential target of the copy-number alteration. These genes, which have
240 been previously associated as driver genes in NET and/or pan-cancer cohorts^{3,5,14}, are shown
241 in **figure 3** for all mNEN with a distinction between mNEC and mNET. We detected several
242 previously known tumor suppressors and oncogenes such as *TP53*, *KRAS*, *MEN1*, *RB1*,
243 *CDKN1B*, *DAXX* and *APC* enriched with non-synonymous mutations ($q \leq 0.05$) as well two
244 additional genes (*SETD2* and *CREBBP*) just above the statistical threshold value ($q \leq 0.1$). By
245 overlapping known drivers within the observed focal amplification and deletion peaks, we
246 detect a plethora of putative drivers with copy-number alteration; such as deletions of
247 *TP53*, *CDKN2A*, *CDKN2B*, *CDKN1B*, *PTPRD*, *CBFA2T3*, *PLCG2*, *ANKDR11*, *IRF8*, *LINC01237*,
248 *PRKN*, *ZNF407*, common fragile sites such as *DMD*, *FHIT* and *MACROD2*, and amplifications
249 of genes such as *PCAT1/MYC* and *MDM2*. Furthermore, focal deletions of additional genes
250 such as *CAMTA1*, *DLUE1/2*, *TRIM13*, *KCNRG*, *FXD1* were found in ≤ 2 samples
251 (**supplementary table 1**). Large perturbations on chromosome 12q15 (*MDM2*) were
252 observed within mNEN harboring chromothripsis (**supplementary figure 6**). Furthermore,
253 we could detect a single in-frame fusion of the common fusion-partner *EWSR1* seen in
254 pNET³. Moreover, we observed only two genes harboring hotspot coding mutations (on
255 base-level) which were shared between three samples (*ZNF829* and *KRAS*) and seven genes
256 between two samples (*UHRF1BP1L*, *CDKN1B*, *MEN1*, *LEKR1*, *OR5L1*, *CTNNB1* and *GNAS*;
257 **supplementary table 1**).

258

259 We observed an overall heterogeneous pattern of putative drivers, the most frequently
260 putative driver was found to be *CDKN2A/B* ($n = 18$; 15), followed by *TP53* ($n = 17$), *CDKN1B*
261 ($n = 12$), *PTPRD* ($n = 11$), *KRAS* ($n = 11$), *MEN1* ($n = 11$) and *RB1* ($n = 11$). Strikingly, a
262 significant portion of the total mNEN cohort had no mutual putative driver(s) (9 out of 86;
263 10%) and only contained patient-specific putative drivers.

264

265 We next investigated whether any form of mutational enrichment, such as somatic
266 alterations within certain genes (mutations and/or copy-number alterations) or evidence of
267 large-scale events (kataegis and chromothripsis), could be related to one of our three major
268 subgroups relating to subtype or primary localization; being mNEC ($n = 16$), pancreas- ($n =$
269 20) and midgut-derived mNET ($n = 40$). Using a one-sided Fisher's Exact Test (with
270 Benjamini-Hochberg correction), we detected the enrichment of at least one such event(s)
271 within these subgroups (**supplementary figure 9e**). Within mNEC, an enrichment of
272 alterations within *TP53* (88% of mNEC), *KRAS* (50%), *RB1* (50%), *MYC* (31%), *APC* (31%),
273 *ZFHX4* (31%), *UBR5* (25%) and presence of kataegis (31%) could be appreciated ($q \leq 0.05$).
274 Likewise, within pancreas-derived mNET, an enrichment of was seen for *MEN1* (40% of
275 pancreas-derived mNET), *ATRX* (25%), *DAXX* (25%), *SETD2* (25%) and *PCNT* (20%) whilst
276 midgut-derived mNET revealed enrichment of *CDKN1B* alterations (25% of midgut-derived
277 mNET).

278 **Genomic differences relating to primary localization of mNET**

279 Due to distinct prognosis and previous genetic associations, we investigated genome-wide
280 differences in regards to primary localization within the mNET population ($n = 70$). We
281 observed several genome-wide differences relating to primary localization (**Figure 2,**
282 **Supplementary figure 9**), such as the median genome-wide TMB; ranging from 1.05 (mNET -
283 Midgut; Q_1 - Q_3 : 0.75 - 1.39) and 1.07 (mNET - Unknown; Q_1 - Q_3 : 0.84 - 1.53) to 1.27 (mNET -
284 Other; Q_1 - Q_3 : 1.10 - 1.44) and 1.35 (mNET - Pancreas; Q_1 - Q_3 : 0.9 - 2.12). A similar pattern
285 was detected regarding the number of distinct genes with coding mutations. Midgut-
286 derived mNET also presented a surprisingly low number of structural variants compared to
287 the other mNET sub-populations.

288

289 Next, we investigated possible differences in putative drivers between our major mNET sub-
290 populations, being midgut- ($n = 40$) and pancreas-derived ($n = 20$) mNET (**Figure 4,**
291 **supplementary figure 9**). The copy-number profiles (GISTIC2) of both populations differed,
292 in which midgut-derived mNET presented focal deletion peaks at 9p21 (*CDKN2A/B*), 11q23
293 (131 genes), 12p13 (*CDKN1B*), 13q14 (10 driver genes), 14q24 (17 genes) and 16q23 (234
294 genes; common fragile site) coupled with an overall flat diploid profile. Pancreas-derived

295 mNET presented a different profile harboring focal deletion peaks at 2q37 (*LINC01237*,
296 *LINC01880*, *LINC01238*), 9p21 (*CDKN2A/B*) and Xp21 (*DMD*; common fragile site gene)
297 couples with a more instable genomic profile, including several samples with large-scale
298 chromosomal losses (**supplementary figure 8**, **supplementary figure 9c**). When
299 investigating the statistically significant large-scale copy-number alterations of the
300 chromosomal arms, we also detect striking differences between the major subgroups
301 (**supplementary figure 10**). Within mNEC, we detected a large number of samples (69%)
302 harboring a loss of 22_q. Midgut-derived mNET revealed amplifications of chromosome 4_{p/q},
303 5_{p/q}, 7_{p/q}, 10_{p/q}, 14_{p/q}, 20_{p/q} and loss of 9_{p/q} in various samples (~30%) and a loss of 18_{p/q} in
304 66% of samples. This re-confirms the high frequency of chromosome 18 loss in midgut-
305 derived NET and the association with *DDC*²⁶, as *DCC* is the most recurrently mutated gene
306 on chromosome 18 in our cohort also ($n = 5$). Finally, over half of pancreas-derived mNET
307 revealed amplifications of chromosome 5_{p/q}, 7_{p/q}, 9_q, 12_{p/q}, 13_q, 14_{p/q}, 17_{p/q}, 18_{p/q}, 19_{p/q}, 20_{p/q}
308 and loss of 22_q.

309

310 Unbiased driver gene analysis (dN/dS) on midgut-derived mNET presented *CDKN1B* whilst
311 pancreas-derived mNET revealed *MEN1*, *DAXX* and *SETD2*. Several genes (present in ≥ 3
312 samples) were found only, or predominately, within midgut-derived mNET: *CDKN1B*,
313 *CDKN2A / CDKN2B*, *BIRC7*, *GNAS*, *PSIP1*, *KMT2A* and *PTPRD* (**figure 4**). Conversely, *MEN1*,
314 *DAXX*, *SETD2*, *CREBBP*, *PCNT*, *KDR* and *TSC2* were found to be mutated only within pancreas-
315 derived mNET. Moreover, *MEN1* was found to be mutationally enriched within pancreas-
316 derived mNET when compared to the entire mNEN cohort ($q \leq 0.05$). Several midgut-
317 derived mNET ($n = 9$; 23%) did not readily present a shared mutual driver and only harbored
318 somatic mutations in private or as-of-yet unassociated cancer driver genes.

319 **Clinically-actionable mutations.**

320 We observed forty-two mNEN (49%) harboring one or more target-specific or general
321 somatic aberrations which are known as possible (and responsive) druggable targets against
322 currently-available (or under development) treatment agents are available. Twenty-one
323 mNEN (24%) harbored somatic aberrations corresponding to a treatment that is currently
324 registered for NEN or specifically for the NEN-subtype of that particular patient (**figure 5**,
325 **supplementary table 1**). In addition, twelve patients (14%) could benefit from therapies that

326 are off-label, but are commonly considered best practice for NEN. Another eight patients
327 (9%) could benefit from drugs which are registered for another indication but not currently
328 administered in NEN treatment. Additionally, six tumors harbored an aberration rendering
329 them sensitive to a drug that is still in development; including a single patient with no
330 actionable alterations otherwise. We found *RB1* ($n = 11$), *KRAS* ($n = 11$), *MTAP* ($n = 5$), high-
331 TMB (≥ 10 ; $n = 5$), *RICTOR* ($n = 4$) and *TP53* ($n = 4$) to be the most frequently observed
332 (target-specific or general) somatic aberrations which granted eligibility to various possible
333 treatment options. In total, ten midgut-derived mNET (25%) and eleven pancreas-derived
334 mNET (55%) revealed potentially responsive alterations in various genes and most strikingly,
335 almost all mNEN (94%) revealed potential responsive targets due to *RB1* and/or *KRAS*
336 mutations or towards checkpoint inhibitors due to high tumor mutational burden (≥ 10).

337 **Discussion**

338 Historically, NEN has long been known as a difficult malignancy to diagnose, monitor and
339 treat due to presentation of an inherently wide spectrum of disease progression, cellular
340 differentiation and low mutational burden, resulting in few targetable mutations and a
341 relatively stable tumor genome. Indeed, mNET is characterized by the lowest TMB of all
342 metastatic cohorts sequenced within the CPCT-02 study.¹⁴ This study is the first to have an
343 in-depth look into the whole genome and mutations of a large cohort of 86 metastatic NEN
344 from various primary localizations and differentiation grade. The relatively large number of
345 unknown primary tumor localizations in this mNEN cohort ($n = 12$; 14%) reflects the
346 difficulties in daily clinical practice to determine the site of origin for mNEN.

347

348 In our mNEN cohort, it is apparent that the molecular landscape of mNEC is markedly
349 dissimilar from the more differentiated mNET, in terms of mutational burden (median TMB
350 of 5.45 vs. 1.08, respectively), genomic stability, and distinct mutant (driver) genes. With
351 respect to TMB, four mNEC and a single mNET presented a high-TMB genotype (TMB ≥ 10)
352 which could render these patients eligible for immune-based therapies such as checkpoint
353 inhibitors.^{27,28}

354

355 The single high-TMB pancreas-derived mNET presented a striking contribution of the
356 mutational signature associated with alkylating agents (temozolomide) and was previously

357 treated with a combination of 5-fluorouracil and the alkylating antineoplastic agent
358 streptozotocin. The mechanism of action for streptozocin closely resembles that of
359 temozolomide as both react with DNA by undergoing substitution reactions forming a
360 methyl diazonium ion, resulting in methylation of primarily N⁷ guanine (67%). They both
361 induce high levels of DNA methylation, and recognition and repair of this methylation
362 results in single- and double-strand DNA breaks.²⁹ To the best of our knowledge, no data
363 have been published on a correlation between hypermutation and streptozocin treatment,
364 but as streptozocin and temozolomide so closely resemble each other in their mechanism of
365 action, one can hypothesize the same mechanism to occur in streptozocin-treated patients.
366 It would be interesting to investigate whether prior treatment with streptozocin or
367 temozolomide indeed induces high TMB in mNEN, and if so, whether pretreatment with
368 streptozocin or temozolomide renders these tumors more sensitive to checkpoint inhibition.
369 Similarly, we observed a large contribution of the mutational signature associated with base
370 excision repair deficiency due to *MUTYH* aberrations in the second highest-TMB mNET, and
371 indeed this patient harbored a pathogenic germline *MUTYH* allele coupled with a complete
372 somatic loss of the respective chromosomal arm. *MUTYH* abnormalities have also previously
373 described to occur in pancreatic NET.³ A single mNET presented a *BRCA2*-genotype
374 associated with homologous recombination deficiency but did not harbor (somatic)
375 mutations within *BRCA2*. It did harbor a somatic mutation in *RAD51C*, a gene known to be
376 involved with homologous recombination and repair of DNA.

377

378 Concerning genomic stability, we observed evidence of chromothripsis, a large-scale and
379 catastrophic chromosomal rearrangement, within six mNEN (four mNEC, two mNET).
380 Strikingly, four out of six chromothripsis events occurred on chromosome 12. In addition,
381 we observe the first occurrence of localized hypermutation (kataegis) in six mNEC. Kataegis
382 encompasses a pattern of localized hypermutations, which has been identified in various,
383 but not all and to a varying degree, cancer types.^{30,31} These regions of kataegis often co-
384 localize with regions of genetic rearrangements. Kataegis is thought to arise from frequent
385 genomic C-to-U deamination events as a result of APOBEC-family enzyme activity, a DNA
386 cytosine deaminase which was recently identified as an internal and thus far unrecognized
387 source of DNA damage and mutagenesis in various cancer types.³² More recently, kataegis,
388 rather than tumor mutational burden, microsatellite instability or mismatch repair

389 deficiency, was found to independently correlate with PD-L1/PD-L2 expression, and could
390 thus be a marker in response to immune checkpoint inhibition.³³

391

392 Using unbiased driver gene analysis (dN/dS and GISTIC2) on the mNEN cohort, and on
393 mNEC/mNEC separately to explore putative driver genes, we (re-)discovered 9 genes to be
394 enriched with non-synonymous mutations (*TP53*, *CDKN1B*, *KRAS*, *MEN1*, *RB1*, *CREBBP*, *APC*,
395 *DAXX* and *SETD2*) and detected 17 focal deletion and 2 focal amplification peaks overlapping
396 with a plethora of (driver) genes, including deletions of *TP53*, *CDKN2A*, *CDKN2B*, *CDKN1B*,
397 *PTPRD*, *CBFA2T3*, *PLCG2*, *ANKDR11*, *IRF8*, *LINC01237*, *PRKN*, *ZNF407* and fragile site genes
398 *FHIT*, *DMD* and *MACROD2*, and amplifications of *PCAT1/MYC* and *MDM2*. Investigation of
399 mutational enrichment within our major subgroups revealed that somatic alterations in
400 *TP53*, *KRAS*, *RB1*, *MYC*, *APC*, *ZFH4* and *UBR5*, as well as presence of kataegis was enriched
401 within mNEC. Within pancreas-derived mNET, we report the enriched presence of mutant
402 *MEN1*, *ATRX*, *DAXX*, *SETD2* and *PCNT* whilst midgut-derived mNET showed preference for
403 *CDKN1B* alterations.

404

405 Of the genetic alterations named above, a number have been previously associated with
406 midgut NET (*CDKN1B*)^{34,35}, lung NET (*FHIT*)³⁶⁻³⁸, pancreas NET (*TP53*, *MEN1*, *DAXX* and
407 *SETD2*)³⁹ and NEC (*TP53* and *RB1*)^{40,41}. Other genes are associated with various other
408 malignancies (*PTPRD*³⁶, *CBFA2T3*⁴², *ANKRD11*⁴³⁻⁴⁵, *ZFH4*⁴⁶ and *MDM2*⁴⁷) or genomic
409 instability (*DMD* and *PRKN*³⁷, *MACROD2*)⁴⁸. Deletion of *PGLC2* has been linked to
410 irregularities within the immune system.⁴⁹ *DAXX* is a tumor suppressor gene, its protein
411 functioning as a dimer together with *ATRX* involved in chromatin stabilization.⁵⁰ Loss of
412 function mutations in *DAXX* have been associated with an increased risk of liver
413 metastases⁵¹ and with shortened overall survival²⁵. Conversely, in a series of 58 pNET, of
414 which 17 had a somatic *DAXX* mutation, the presence of a *DAXX* mutation was associated
415 with a favorable prognosis, as was the presence of a *MEN1* mutation³⁹. In addition,
416 mutations in *TP53*, *APC*, *KRAS* and *RB1* has previously been associated with pancreatic or
417 colorectal NEN and small cell lung carcinoma (SCLC)⁵²⁻⁵⁴, and amplification of *MYC* has been
418 found in SCLC with neuroendocrine differentiation⁵⁵.

419

420 Currently, the choice of treatment in an individual mNEN patient is, besides factors such as
421 comorbidity and patient preference, determined by primary tumor localization, proliferation
422 index (as determined by Ki-67 or MIB-1 staining) and somatostatin expression. The
423 distinction based on primary tumor localization stems from the different embryologic
424 structures the tumor can originate from (foregut, midgut or hindgut). When we compared
425 the various origins at a genomic level, we could observe an increasing TMB; ranging from
426 1.05 (mNET - Midgut; Q₁-Q₃: 0.75 - 1.39) and 1.07 (mNET - Unknown; Q₁-Q₃: 0.84 - 1.53) to
427 1.27 (mNET - Other; Q₁-Q₃: 1.10 - 1.44) and 1.35 (mNET - Pancreas; Q₁-Q₃: 0.9 - 2.12) to 5.45
428 (mNEC; Q₁-Q₃: 3.8 - 8.85). In addition, when we compared the two largest groups of mNET
429 per primary localization (midgut and pancreas), we can readily distinguish between the two
430 subtypes based on somatic mutation and copy-number profiles. Yet strikingly, many midgut-
431 derived mNET (*n* = 9; 23%) did not present a mutual driver gene but each was characterized
432 by distinct sets of mutated genes reflecting the heterogenous nature of the malignancy.

433

434 Almost half of mNEN (*n* = 42; 49%) harbored a specific genomic alteration or genotype for
435 which an FDA-approved drug is currently available, either on (registered for that indication)
436 or off-label. Thus, whole genome sequencing of metastatic lesions revealed 49% of mNEN
437 patients harboring clinically-relevant targetable somatic aberrations which could possibly
438 extend their treatment-repertoire. Additionally, six patients' tumors (also) harbored a
439 specific genomic alteration which could render them sensitive to drugs that are currently
440 under development in clinical trials. These drugs are currently not readily available for these
441 patients, but could provide new treatment options in the future. When deciding upon a new
442 line of systemic treatment, a metastatic biopsy could always be considered, preferably in
443 the context of a study, as this could shed light upon additional and effective treatment
444 options for these late-stage patients with otherwise few remaining treatment options. In
445 the Netherlands, we have the DRUP study active, a study in which patients for whom no
446 standard treatments are currently available and whom might be treated with anticancer
447 treatments outside of their approved label based on the presence of actionable mutations
448 in their tumors.⁵⁶

449

450 In this current study exploring the largest whole-genome sequenced mNEN repository to
451 date (*n* = 86), we focused on the genes that drive mNEN and analyzed additional aspects of

452 genomic instability within mNEN, such as structural variants, kataegis, chromothripsis and
453 homologous recombination deficiency. With increased knowledge and new algorithms on
454 analyzing and interpreting large-scale WGS cohorts, our understanding of the complex
455 molecular makeup of (m)NEN has been greatly increased and could be exploited for better
456 distinction of tumor subgroups and new treatment options.

457 **Online methods**

458 **Patient cohort and study procedures**

459 Patients with mNEN were recruited under the study protocol (NCT01855477) of the Center
460 for Personalized Cancer Treatment (CPCT) within the CPCT-02 study. This CPCT-02 protocol
461 was approved by the medical ethical committee (METC) of the University Medical Center
462 Utrecht. Patients were eligible for inclusion if the following criteria were met: 1) age \geq 18
463 years; 2) locally advanced or metastatic solid tumor; 3) indication for new line of systemic
464 treatment with registered anti-cancer agents; 4) safe biopsy according to the intervening
465 physician. All patients provided written informed consent before any study procedure. The
466 study procedures consisted of the collection of matched peripheral blood samples for
467 reference DNA and image-guided percutaneous biopsy of the metastatic lesion. For the
468 current study, patients were included for biopsy between May 10th 2016 and July 17th 2018
469 resulting in a cohort of 86 distinct patients from 13 Dutch hospitals (**Supplementary table**
470 **1**).

471 **Collection, sequencing and processing of mNEN biopsies.**

472 Blood samples were collected in CellSave preservative tubes (Menarini-Silicon Biosystems,
473 Huntington Valley, PA, USA) and shipped by room temperature to the central sequencing
474 facility at the Hartwig Medical Foundation. Tumor samples were fresh-frozen in liquid
475 nitrogen directly after the procedure and send to a central pathology tissue facility. Tumor
476 cellularity was estimated by assessing a hematoxylin-eosin (HE) stained 6 micron section.
477 Subsequently, 25 sections of 20 micron were collected for DNA isolation. DNA was isolated
478 with an automated workflow (QiaSymphony) using the DSP DNA Midi kit for blood and
479 QIASymphony DSP DNA Mini kit for tumor samples according to the manufacturer's protocol
480 (Qiagen). DNA concentration was measured by Qubit™ fluorometric quantitation
481 (Invitrogen, Life Technologies, Carlsbad, CA, USA). DNA libraries for Illumina sequencing
482 were generated from 50-100 ng of genomic DNA using standard protocols (Illumina, San
483 Diego, CA, USA) and subsequently whole-genome sequenced in a HiSeq X Ten system using
484 the paired-end sequencing protocol (2x150bp) for both the metastatic tumor and matched
485 blood sample.

486

487 Subsequent alignment, somatic mutation detection and *in silico* tumor cell percentage
488 estimation were performed in a uniform manner as detailed by Priestley et al. (2019).¹⁴
489 Briefly, paired-end sequencing reads were aligned against the human reference genome
490 (GRCh37) using BWA-mem (v0.7.5a).⁵⁷ Duplicate reads were marked and small insertion and
491 deletions (InDels) were realigned using GATK IndelRealigner (v3.4.46). Prior to somatic SNV
492 and InDel variant calling, base qualities were recalibrated using GATK BQSR (v3.4.46).⁵⁸
493 Somatic SNV, InDels and MNV were called by Strelka (v1.0.14) using the matched peripheral
494 blood WGS sample for matched-normal variant calling.⁵⁹

495

496 Additional in-depth settings and optimizations of the HMF pipeline are described by
497 Priestley et al. (2019) and tools are available at <https://github.com/hartwigmedical/>.

498

499 The somatic mutations (SNV, InDels and MNV) were further annotated with Ensembl Variant
500 Effect Predictor⁶⁰ (VEP, version 99, cache 99_GRCh37) using GENCODE (v33) annotations in
501 tandem with the dbNSFP⁶¹ plugin (version 3.5, hg19) for gnomAD⁶² population frequencies.
502 SIFT⁶³ and PolyPhen-2⁶⁴ scoring was applied for additional functional effect prediction.

503

504 During downstream analysis, we only retained SNV, InDels and MNV which passed all of the
505 following heuristic filters; default Strelka filters (PASS-only), gnomAD exome (ALL) allele
506 frequency < 0.001, gnomAD genome (ALL) < 0.005, not present in ≥ 5 samples from the
507 Hartwig Medical Foundation germline panel-of-normals (GATK Haplotype) and not present
508 in ≥ 3 samples from the Hartwig Medical Foundation Strelka-specific somatic blacklist.

509

510 Putative protein-altering (coding) or high-impact (e.g. splicing) mutations were aggregated
511 per sample and gene by selecting the most deleterious annotated effect (from VEP) on any
512 known overlapping gene-wise transcript (except those transcripts flagged as retained intron
513 and nonsense mediated decay). In addition, structural variants with a Tumor Allele
514 Frequency (TAF) ≥ 0.1 that overlapped only partly with the respective coding sequences (i.e.
515 not all exons of the respective gene), were annotated as 'Structural Variant' mutations.
516 Multiple coding mutations and/or SV per gene were annotated as 'multiple mutations'.

517

518 Discovery of somatic structural variants (SV), copy-number alterations and in-frame fusions
519 of *EWSR1* was performed using the GRIDDS, PURPLE and LINX suite.⁶⁵ During the
520 downstream analyses, we only retained somatic structural variants passing all default QC
521 filters (PASS-only) and with an upstream and/or downstream TAF ≥ 0.1 .

522

523 Mean read coverages of the reference and tumor samples were calculated using Picard
524 Tools (v1.141; CollectWgsMetrics) based on GRCh37.⁶⁶ Genomic and coding tumor
525 mutational burden (TMB) was calculated as previously described by van Dessel/van Riet et
526 al. (2019).⁶⁷

527 **Determining purity-corrected allele frequencies for somatic alterations.**

528 To calculate the Tumor Allele Frequencies (TAF) of somatic SNV, InDels, MNV and SV,
529 representing the tumor purity-corrected variant frequencies, we followed a previously
530 described approach by Stephens et al. (2012)⁶⁸, implemented as:

$$531 \quad TAF_m = \frac{f_m}{p} [pC_t + (1 - p)C_h] \text{ (equation 1),}$$

532 in which where f_m is the ratio of primary-aligned and non-duplicated reads observed for
533 alternative allele m over the reference allele (VAF), p is the *in silico* estimated tumor purity
534 fraction, C_t is the absolute copy-number of the segment overlapping m and C_h is the wild-
535 type (healthy) copy number; $C_h = 2$ for autosomes and allosomes in female samples and
536 $C_h = 1$ for allosomes in male samples.

537 **Discovery of genes under evolutionary selection**

538 We performed a dN/dS analysis on somatic mutations (SNV and InDels) using dndscv⁶⁹
539 (v0.0.1.0) on respective genome sequences and transcript annotations using a custom
540 transcript database based on ENSEMBL⁷⁰ Genes (v99)/GENCODE (v33) annotations. We
541 performed a dN/dS analysis over the entire NEN cohort ($n = 86$) and four separate dN/dS
542 analysis on the major subgroups (mNEC; $n = 16$, NET; $n = 70$, mNET-midgut; $n = 40$ and
543 mNET-pancreas; $n = 20$). Genes-of-interest were selected based on the statistical
544 significance, corrected for multiple hypothesis testing (Benjamini-Hochberg), which
545 integrated all mutation types (missense, nonsense, essential splice-site mutations and
546 InDels; qglobal_cv ≤ 0.1) and/or without InDels (qallsubs_cv ≤ 0.1).

547 **Detection and annotation of recurrent copy-number alterations**

548 To detect recurrent copy-number alterations, we performed a GISTIC2⁷¹ (v2.0.23) analysis
549 over the entire mNEN cohort and, again, four separate GISTIC2 analysis on the major
550 subgroups (mNEC, mNET and pancreas- and midgut-derived mNET).

551

552 The GISTIC2 was performed using the following settings:

553 Genes were annotated to GISTIC2 peaks ($q \leq 0.1$) based on the following strategy;

- 554 1) GISTIC2 focal peaks (all_lesions.conf_95.txt) were overlapped to genes (from verified
555 and manually annotated loci, no pseudogenes or read-throughs and from standard
556 chromosomes; $n = 36574$) from GENCODE (GRCh37; v33), taking into consideration
557 only the genes overlapping with at least 100 base pairs within the detected GISTIC2
558 peak.
- 559 2) If a GISTIC2 focal peak overlapped with multiple GENCODE genes, a combined
560 database containing known drivers detected in a metastatic pan-cancer dataset
561 (CPCT-02)¹⁴, COSMIC Cancer Gene Census (v85)⁷², OncoKB Cancer Gene Census (June
562 2019)⁷³, Martincorena et al. (2017)⁶⁹ and Priestley et al. (2019)¹⁴ were used to
563 further pinpoint the possible target gene(s) ($n = 1272$), e.g. if a GISTIC2 peak
564 overlapped both *PTEN* and near-adjacent non-driver gene, only *PTEN* would be
565 chosen as possible target. The list of all overlapping GENCODE⁷⁴ (v33) genes per
566 GISTIC2 peak can be found in [supplementary table 1](#).
- 567 3) If no overlapping genes were found, GISTIC2 peaks were annotated with the nearest
568 GENCODE (v33) protein-coding gene ($n = 19988$).

569 **Mutational signature analysis**

570 Mutational signatures based on the trinucleotide contexts of SNVs was performed, mainly
571 using the MutationalPatterns package (1.10.0)⁷⁵ and as previously described.⁶⁷ The 96 Single
572 Base Substitution (SBS) mutational signatures (COSMIC v3) as established by Alexandrov et
573 al. (2019)²³, (matrix S_{ij} ; $i = 96$; number of trinucleotide motifs; $j =$ number of signatures)
574 were downloaded from COSMIC (as deposited on May 2019). The proposed etiology of each
575 SBS signature was derived from Alexandrov et al. (2019)²³, Petljak et al. (2019)²³, Angus et
576 al. (2019)⁶ and Christensen et al. (2019)⁷⁶.

577

578 In addition, *de novo* mutational signature analysis by MutationalPatterns was performed
579 based on the max. number of relevant signatures as assessed using the NMF R package⁷⁷
580 (v0.21.0) with 1000 iterations (**supplementary figure 7d**). By comparing the cophenetic
581 correlation coefficient, residual sum of squares and silhouette, we opted to generate seven
582 custom *de novo* signatures. Custom signatures were correlated to existing (COSMIC v3)
583 mutational signatures using cosine similarity.

584 **Detection of chromothripsis**

585 Shatterseek¹⁸ (v0.4) using default parameters was used to detect chromothripsis-like
586 events. As input, we used the rounded absolute copy numbers (as derived by PURPLE) and
587 structural variants with an TAF ≥ 0.1 at either end of the breakpoint. The male sex
588 chromosome (chrY) was excluded. The criteria for a chromothripsis-like event were based
589 on the following criteria: a) total number of intra-chromosomal structural variants involved
590 in the event ≥ 25 ; b) max. number of oscillating CN segments (2 states) ≥ 7 or max. number of
591 oscillating CN segments (3 states) ≥ 14 ; c) total size of chromothripsis event ≥ 20 megabase
592 pairs (Mbp); d) satisfying the test of equal distribution of SV types ($p > 0.05$); and e)
593 satisfying the test of non-random SV distribution within the cluster region or chromosome
594 ($p \leq 0.05$).

595 **Classification of homologous recombination deficiency genotypes**

596 To determine Homologous Recombination Deficiency (HRD) due to possible loss-of-function
597 of *BRCA1* and/or *BRCA2* (amongst others), we utilized the Classifier for Homologous
598 Recombination Deficiency with default settings (CHORD; v2.0). CHORD uses a random-forest
599 approach to classify samples into HR-deficient / HR-proficient categories.⁷⁸

600 **Inventory of clinically-actionable somatic alterations and putative therapeutic targets**

601 Current clinical relevance of somatic alterations in relation to putative treatment options or
602 resistance mechanisms and trial eligibility was determined based upon the following
603 databases; CiViC⁷⁹ (Nov. 2018), OncoKB⁷³ (Nov. 2018), CGI⁸⁰ (Nov. 2018) and the iClusion
604 (Dutch) clinical trial database (Sept. 2019) from iClusion (Rotterdam, the Netherlands). The
605 databases were aggregated and harmonized using the HMF knowledgebase-importer (v1.7).
606 This list was manually corrected for discrepancies and subsequently, we curated the linked
607 putative treatments for current on- and off-label mNEN and mNEN-subtype treatment

608 options, as defined within the Netherlands by the Dutch Medicines Evaluation Board
609 (“College ter Beoordeling van Geneesmiddelen; CBG”).⁸¹

610 **Data availability**

611 WGS data and corresponding clinical data have been requested from Hartwig Medical
612 Foundation and provided under data request number DR-036. Both WGS and clinical data is
613 freely available for academic use from the Hartwig Medical Foundation through
614 standardized procedures and request forms can be found at
615 <https://www.hartwigmedicalfoundation.nl>.¹⁴ No additional data were used for this study.

616 **Code availability**

617 Analysis and visualization have been performed using the statistical platform language R
618 (3.6.2), all utilized custom code and scripts can be freely requested and distributed by
619 contacting the authors.

620 References

- 621 1. Bosman, F. T. WHO classification of tumours of the digestive system - NLM Catalog - NCBI. in *WHO*
622 *classification of tumours of the digestive system* (2010).
- 623 2. Cheng, J. *et al.* Pan-cancer analysis of homozygous deletions in primary tumours uncovers rare tumour
624 suppressors. *Nat. Commun.* (2017) doi:10.1038/s41467-017-01355-0.
- 625 3. Scarpa, A. *et al.* Whole-genome landscape of pancreatic neuroendocrine tumours. *Nature* (2017)
626 doi:10.1038/nature21063.
- 627 4. Do, H. K. *et al.* Allelic alterations in well-differentiated neuroendocrine tumors (carcinoid tumors)
628 identified by genome-wide single nucleotide polymorphism analysis and comparison with pancreatic
629 endocrine tumors. *Genes Chromosom. Cancer* (2008) doi:10.1002/gcc.20510.
- 630 5. Banck, M. S. *et al.* The genomic landscape of small intestine neuroendocrine tumors. *J. Clin. Invest.*
631 (2013) doi:10.1172/JCI67963.
- 632 6. Angus, L. *et al.* The genomic landscape of metastatic breast cancer highlights changes in mutation and
633 signature frequencies. *Nat. Genet.* (2019) doi:10.1038/s41588-019-0507-7.
- 634 7. Brown, D. *et al.* Phylogenetic analysis of metastatic progression in breast cancer using somatic
635 mutations and copy number aberrations. *Nat. Commun.* (2017) doi:10.1038/ncomms14944.
- 636 8. Navin, N. *et al.* Tumour evolution inferred by single-cell sequencing. *Nature* (2011)
637 doi:10.1038/nature09807.
- 638 9. Hunter, K. W., Amin, R., Deasy, S., Ha, N. H. & Wakefield, L. Genetic insights into the morass of
639 metastatic heterogeneity. *Nature Reviews Cancer* (2018) doi:10.1038/nrc.2017.126.
- 640 10. Walter, D. *et al.* Genetic heterogeneity of primary lesion and metastasis in small intestine
641 neuroendocrine tumors. *Sci. Rep.* (2018) doi:10.1038/s41598-018-22115-0.
- 642 11. Wong, H. L. *et al.* Molecular characterization of metastatic pancreatic neuroendocrine tumors (PNETs)
643 using whole-genome and transcriptome sequencing. *Cold Spring Harb. Mol. Case Stud.* (2018)
644 doi:10.1101/mcs.a002329.
- 645 12. Cho, S. Y. *et al.* Cervical small cell neuroendocrine tumor mutation profiles via whole exome
646 sequencing. *Oncotarget* (2017) doi:10.18632/oncotarget.14098.
- 647 13. Shen, P. *et al.* Comprehensive genomic profiling of neuroendocrine bladder cancer pinpoints molecular
648 origin and potential therapeutics. *Oncogene* (2018) doi:10.1038/s41388-018-0192-5.
- 649 14. Priestley, P. *et al.* Pan-cancer whole-genome analyses of metastatic solid tumours. *Nature* (2019)
650 doi:10.1038/s41586-019-1689-y.
- 651 15. Alexandrov, L. B. *et al.* Signatures of mutational processes in human cancer. *Nature* **500**, 415–421
652 (2013).
- 653 16. Prakash, R., Zhang, Y., Feng, W. & Jasin, M. Homologous recombination and human health: The roles of
654 BRCA1, BRCA2, and associated proteins. *Cold Spring Harb. Perspect. Biol.* (2015)
655 doi:10.1101/cshperspect.a016600.
- 656 17. Chan, K. *et al.* An APOBEC3A hypermutation signature is distinguishable from the signature of
657 background mutagenesis by APOBEC3B in human cancers. *Nat. Genet.* **47**, 1067–1072 (2015).

- 658 18. Cortés-ciriano, I., Lee, J., Xi, R., Jain, D. & Jung, Y. L. Comprehensive analysis of chromothripsis in 2 , 658
659 human cancers using whole-genome sequencing. (2018).
- 660 19. Rausch, T. *et al.* Genome sequencing of pediatric medulloblastoma links catastrophic DNA
661 rearrangements with TP53 mutations. *Cell* (2012) doi:10.1016/j.cell.2011.12.013.
- 662 20. Sanborn, J. Z. *et al.* Double minute chromosomes in glioblastoma multiforme are revealed by precise
663 reconstruction of oncogenic amplicons. *Cancer Res.* (2013) doi:10.1158/0008-5472.CAN-13-0186.
- 664 21. Alexandrov, L. B., Nik-Zainal, S., Wedge, D. C., Campbell, P. J. & Stratton, M. R. Deciphering Signatures
665 of Mutational Processes Operative in Human Cancer. *Cell Rep.* **3**, 246–259 (2013).
- 666 22. Alexandrov, L. B. *et al.* The Repertoire of Mutational Signatures in Human Cancer. *bioRxiv* (2019)
667 doi:10.1101/322859.
- 668 23. Petljak, M. *et al.* Characterizing Mutational Signatures in Human Cancer Cell Lines Reveals Episodic
669 APOBEC Mutagenesis. *Cell* (2019) doi:10.1016/j.cell.2019.02.012.
- 670 24. David, S. S., O’Shea, V. L. & Kundu, S. Base-excision repair of oxidative DNA damage. *Nature* (2007)
671 doi:10.1038/nature05978.
- 672 25. Pea, A. *et al.* Genetic Analysis of Small Well-differentiated Pancreatic Neuroendocrine Tumors
673 Identifies Subgroups With Differing Risks of Liver Metastases. *Ann. Surg.* (2018)
674 doi:10.1097/sla.0000000000003022.
- 675 26. Nieser, M. *et al.* Loss of Chromosome 18 in Neuroendocrine Tumors of the Small Intestine: The Enigma
676 Remains. *Neuroendocrinology* (2017) doi:10.1159/000446917.
- 677 27. Samstein, R. M. *et al.* Tumor mutational load predicts survival after immunotherapy across multiple
678 cancer types. *Nature Genetics* (2019) doi:10.1038/s41588-018-0312-8.
- 679 28. Chan, T. A. *et al.* Development of tumor mutation burden as an immunotherapy biomarker: Utility for
680 the oncology clinic. *Annals of Oncology* (2019) doi:10.1093/annonc/mdy495.
- 681 29. Li, G. M. Mechanisms and functions of DNA mismatch repair. *Cell Research* (2008)
682 doi:10.1038/cr.2007.115.
- 683 30. Yousif, F. *et al.* The Origins and Consequences of Localized and Global Somatic Hypermutation. *bioRxiv*
684 287839 (2018) doi:10.1101/287839.
- 685 31. Nik-Zainal, S. *et al.* Mutational processes molding the genomes of 21 breast cancers. *Cell* **149**, 979–993
686 (2012).
- 687 32. Harris, R. S. Molecular mechanism and clinical impact of APOBEC3B-catalyzed mutagenesis in breast
688 cancer. *Breast Cancer Research* (2015) doi:10.1186/s13058-014-0498-3.
- 689 33. Boichard, A., Tsigelny, I. F. & Kurzrock, R. High expression of PD-1 ligands is associated with kataegis
690 mutational signature and APOBEC3 alterations. *Oncoimmunology* **6**, e1284719 (2017).
- 691 34. Francis, J. M. *et al.* Somatic mutation of CDKN1B in small intestine neuroendocrine tumors. *Nat. Genet.*
692 (2013) doi:10.1038/ng.2821.
- 693 35. Alrezk, R., Hannah-Shmouni, F. & Stratakis, C. A. MEN4 and CDKN1B mutations: the latest of the MEN
694 syndromes. *Endocr. Relat. Cancer* (2017) doi:10.1530/erc-17-0243.
- 695 36. Veeriah, S. *et al.* The tyrosine phosphatase PTPRD is a tumor suppressor that is frequently inactivated

- 696 and mutated in glioblastoma and other human cancers. *Proc. Natl. Acad. Sci. U. S. A.* (2009)
697 doi:10.1073/pnas.09005711106.
- 698 37. Mitsui, J. *et al.* Mechanisms of genomic instabilities underlying two common fragile-site-associated
699 Loci, PARK2 and DMD, in germ cell and cancer cell lines. *Am. J. Hum. Genet.* (2010)
700 doi:10.1016/j.ajhg.2010.06.006.
- 701 38. Duan, H. *et al.* PARK2 suppresses proliferation and tumorigenicity in non-small cell lung cancer. *Front.*
702 *Oncol.* (2019) doi:10.3389/fonc.2019.00790.
- 703 39. Zhang, J. *et al.* Current understanding of the molecular biology of pancreatic neuroendocrine tumors.
704 *Journal of the National Cancer Institute* (2013) doi:10.1093/jnci/djt135.
- 705 40. Tang, L. H. *et al.* Well-differentiated neuroendocrine tumors with a morphologically apparent high-
706 grade component: A pathway distinct from poorly differentiated neuroendocrine carcinomas. *Clin.*
707 *Cancer Res.* (2016) doi:10.1158/1078-0432.CCR-15-0548.
- 708 41. Jiao, Y. *et al.* DAXX/ATR, MEN1, and mTOR pathway genes are frequently altered in pancreatic
709 neuroendocrine tumors. *Science (80-)*. (2011) doi:10.1126/science.1200609.
- 710 42. Kochetkova, M. *et al.* CBFA2T3 (MTG16) is a putative breast tumor suppressor gene from the breast
711 cancer loss of heterozygosity region at 16q24.3. *Cancer Res.* (2002).
- 712 43. Neilsen, P. M. *et al.* Identification of ANKRD11 as a p53 coactivator. *J. Cell Sci.* (2008)
713 doi:10.1242/jcs.026351.
- 714 44. Lim, S. P. *et al.* Specific-site methylation of tumour suppressor ANKRD11 in breast cancer. *Eur. J. Cancer*
715 (2012) doi:10.1016/j.ejca.2012.03.023.
- 716 45. Noll, J. E. *et al.* Mutant p53 drives multinucleation and invasion through a process that is suppressed by
717 ANKRD11. *Oncogene* (2012) doi:10.1038/onc.2011.456.
- 718 46. Qing, T. *et al.* Somatic mutations in ZFH4 gene are associated with poor overall survival of Chinese
719 esophageal squamous cell carcinoma patients. *Sci. Rep.* (2017) doi:10.1038/s41598-017-04221-7.
- 720 47. Oliner, J. D., Saiki, A. Y. & Caenepeel, S. The role of MDM2 amplification and overexpression in
721 tumorigenesis. *Cold Spring Harb. Perspect. Med.* (2016) doi:10.1101/cshperspect.a026336.
- 722 48. Sakthianandeswaren, A. *et al.* MACROD2 haploinsufficiency impairs catalytic activity of PARP1 and
723 promotes chromosome instability and growth of intestinal tumors. *Cancer Discov.* (2018)
724 doi:10.1158/2159-8290.CD-17-0909.
- 725 49. Ombrello, M. J. *et al.* Cold urticaria, immunodeficiency, and autoimmunity related to PLCG2 deletions.
726 *N. Engl. J. Med.* (2012) doi:10.1056/NEJMoa1102140.
- 727 50. Dyer, M. A., Qadeer, Z. A., Valle-Garcia, D. & Bernstein, E. ATRX and DAXX: Mechanisms and mutations.
728 *Cold Spring Harb. Perspect. Med.* (2017) doi:10.1101/cshperspect.a026567.
- 729 51. Ziv, E. *et al.* DAXX Mutation Status of Embolization-Treated Neuroendocrine Tumors Predicts Shorter
730 Time to Hepatic Progression. *J. Vasc. Interv. Radiol.* (2018) doi:10.1016/j.jvir.2018.05.023.
- 731 52. Konukiewitz, B. *et al.* Pancreatic neuroendocrine carcinomas reveal a closer relationship to ductal
732 adenocarcinomas than to neuroendocrine tumors G3. *Hum. Pathol.* (2018)
733 doi:10.1016/j.humpath.2018.03.018.

- 734 53. Takizawa, N. *et al.* Molecular characteristics of colorectal neuroendocrine carcinoma; Similarities with
735 adenocarcinoma rather than neuroendocrine tumor. *Hum. Pathol.* (2015)
736 doi:10.1016/j.humpath.2015.08.006.
- 737 54. Shamir, E. R. *et al.* Identification of high-risk human papillomavirus and Rb/E2F pathway genomic
738 alterations in mutually exclusive subsets of colorectal neuroendocrine carcinoma. *Mod. Pathol.* (2019)
739 doi:10.1038/s41379-018-0131-6.
- 740 55. Mollaoglu, G. *et al.* MYC Drives Progression of Small Cell Lung Cancer to a Variant Neuroendocrine
741 Subtype with Vulnerability to Aurora Kinase Inhibition. *Cancer Cell* (2017)
742 doi:10.1016/j.ccell.2016.12.005.
- 743 56. van der Velden, D. L. *et al.* The Drug Rediscovery protocol facilitates the expanded use of existing
744 anticancer drugs. *Nature* (2019) doi:10.1038/s41586-019-1600-x.
- 745 57. Li, H. & Durbin, R. Fast and accurate short read alignment with Burrows-Wheeler transform.
746 *Bioinformatics* **25**, 1754–1760 (2009).
- 747 58. McKenna, A. *et al.* The genome analysis toolkit: A MapReduce framework for analyzing next-
748 generation DNA sequencing data. *Genome Res.* **20**, 1297–1303 (2010).
- 749 59. Kim, S. *et al.* Strelka2: Fast and accurate variant calling for clinical sequencing applications. *doi.org*
750 192872 (2017) doi:10.1101/192872.
- 751 60. McLaren, W. *et al.* The Ensembl Variant Effect Predictor. *Genome Biol.* (2016) doi:10.1186/s13059-016-
752 0974-4.
- 753 61. Liu, X., Wu, C., Li, C. & Boerwinkle, E. dbNSFP v3.0: A One-Stop Database of Functional Predictions and
754 Annotations for Human Nonsynonymous and Splice-Site SNVs. *Hum. Mutat.* (2016)
755 doi:10.1002/humu.22932.
- 756 62. Lek, M. *et al.* Analysis of protein-coding genetic variation in 60,706 humans. *Nature* **536**, 285–291
757 (2016).
- 758 63. Ng, P. C. & Henikoff, S. SIFT: Predicting amino acid changes that affect protein function. *Nucleic Acids*
759 *Res.* (2003) doi:10.1093/nar/gkg509.
- 760 64. Adzhubei, I., Jordan, D. M. & Sunyaev, S. R. Predicting functional effect of human missense mutations
761 using PolyPhen-2. *Curr. Protoc. Hum. Genet.* (2013) doi:10.1002/0471142905.hg0720s76.
- 762 65. Cameron, D. L. *et al.* GRIDSS, PURPLE, LINX: Unscrambling the tumor genome via integrated analysis of
763 structural variation and copy number. *bioRxiv* (2019) doi:10.1101/781013.
- 764 66. Broad Institute. Picard tools. <https://broadinstitute.github.io/picard/>
765 <https://broadinstitute.github.io/picard/%5Cnhttp://broadinstitute.github.io/picard/> (2016).
- 766 67. van Dessel, L. F. *et al.* The genomic landscape of metastatic castration-resistant prostate cancers
767 reveals multiple distinct genotypes with potential clinical impact. *Nat. Commun.* **10**, 546051 (2019).
- 768 68. Stephens, P. J. *et al.* The landscape of cancer genes and mutational processes in breast cancer. *Nature*
769 (2012) doi:10.1038/nature11017.
- 770 69. Martincorena, I. *et al.* Universal Patterns of Selection in Cancer and Somatic Tissues. *Cell* **171**, 1029-
771 1041.e21 (2017).

- 772 70. Zerbino, D. R. *et al.* Ensembl 2018. *Nucleic Acids Res.* (2018) doi:10.1093/nar/gkx1098.
- 773 71. Mermel, C. H. *et al.* GISTIC2.0 facilitates sensitive and confident localization of the targets of focal
774 somatic copy-number alteration in human cancers. *Genome Biol.* **12**, R41 (2011).
- 775 72. Forbes, S. A. *et al.* COSMIC: Somatic cancer genetics at high-resolution. *Nucleic Acids Res.* **45**, D777–
776 D783 (2017).
- 777 73. Chakravarty, D. *et al.* OncoKB: A Precision Oncology Knowledge Base. *JCO Precis. Oncol.* 1–16 (2017)
778 doi:10.1200/PO.17.00011.
- 779 74. Harrow, J. *et al.* GENCODE: The reference human genome annotation for the ENCODE project. *Genome*
780 *Res.* **22**, 1760–1774 (2012).
- 781 75. Blokzijl, F., Janssen, R., van Boxtel, R. & Cuppen, E. MutationalPatterns: Comprehensive genome-wide
782 analysis of mutational processes. *Genome Med.* (2018) doi:10.1186/s13073-018-0539-0.
- 783 76. Christensen, S. *et al.* 5-Fluorouracil treatment induces characteristic T>G mutations in human cancer.
784 *Nat. Commun.* (2019) doi:10.1038/s41467-019-12594-8.
- 785 77. Gaujoux, R. & Seoighe, C. A flexible R package for nonnegative matrix factorization. *BMC*
786 *Bioinformatics* **11**, (2010).
- 787 78. Nguyen, L., Martens, J., Hoeck, A. van & Cuppen, E. Pan-cancer landscape of homologous
788 recombination deficiency. *bioRxiv* (2020) doi:10.1101/2020.01.13.905026.
- 789 79. Griffith, M. *et al.* CIViC is a community knowledgebase for expert crowdsourcing the clinical
790 interpretation of variants in cancer. *Nat. Genet.* **49**, 170–174 (2017).
- 791 80. Tamborero, D. *et al.* Cancer Genome Interpreter annotates the biological and clinical relevance of
792 tumor alterations. *Genome Med.* **10**, 25 (2018).
- 793 81. Pavel, M. *et al.* ENETS consensus guidelines update for the management of distant metastatic disease
794 of intestinal, pancreatic, bronchial neuroendocrine neoplasms (NEN) and NEN of unknown primary
795 site. in *Neuroendocrinology* (2016). doi:10.1159/000443167.
- 796

797 **Acknowledgements**

798 We would like to thank J. (Alberto) G. Nakauma Gonzalez for his assistance in implementing
799 and describing the TAF calculations and iClusion for sharing their data on the association of
800 genetic aberrations to actionable targets and clinical trials.

801 **Grants**

802 N/A.

803 **Author contributions**

804 JVR, BM and HJGVDW wrote the manuscript, which all authors critically reviewed. JVR and
805 HJGVDW performed the bioinformatics analyses. BM managed clinical data assessment. FE,

806 MT, LMV, HK, WD and GV are clinical contributors. MJK is PI of the CPCT-02 study, SS is chair
807 of the CPCT and both supervise the CPCT-02 study. EPJGC coordinated the sequencing of
808 samples and contributed to the bioinformatics analyses.

809 **Competing interests**

810 All authors declare no competing interests.

811 **Additional information**

812 Supplementary information is available for this paper at <https://doi.org/XXXXXXXXXX>.

813 Figures

814 **Figure 1 - Overview of patient inclusion and sub-classification of biopsies.**

815 **a) Flowchart of patient inclusion.** From the CPCT-02 cohort, single biopsies from 86
816 distinct patients with metastatic neuroendocrine neoplasms (mNEN) were selected.
817 From the total pool of available whole-genome sequenced mNET samples. If multiple
818 derived mNET biopsies from the same patient were available, we selected the mNET
819 biopsy with the highest tumor cell purity.

820 **b) Subclassification of mNEN based on primary localization.** The 86 mNEN were
821 subclassified, based on their primary localization, into six major categories; Foregut,
822 Hindgut, Lung, Pancreas and Midgut; whilst samples with indeterminable localization
823 were categorized as Unknown. The number of mNET (in blue) and mNEC (in red) are
824 shown per category.

825 **Figure 2 - Landscape of large-scale genomic alterations detected in mNEN, ordered by** 826 **differentiation grade (NEC / NET) and primary localization.**

827 Overview of genome-wide characteristics of the mNEN cohort ordered by mNEC / mNET and
828 primary localization on decreasing median tumor mutational burden. For each mNEN ($n =$
829 86), the following tracks are shown:

830 **a)** Number of genomic mutations per megabase over the entire genome (TMB); SNV,
831 InDel and MNV are depicted in blue, orange and salmon respectively. Threshold for
832 high-TMB (≥ 10) is shown by a horizontal red dotted line. Y-axis is shown in \log_{10} -
833 scale.

834 **b)** Total number of structural variants including deletions, tandem duplications,
835 translocations, inversions and insertions as detected by GRIDSS. Y-axis is shown in
836 \log_{10} -scale.

837 **c)** Relative frequency of each of the structural variant categories; deletions in orange,
838 tandem duplications in red, translocations in blue, inversions in light-blue and
839 insertions in yellow.

840 **d)** Mean genome-wide ploidy, ranging from 0 (red) to 4 (green; tetraploid). Common
841 diploid status is shown in white.

842 **e)** Relative contribution of the COSMIC single-base substitution mutational signatures
843 (v_3 ; $n = 67$). Signatures with less than 5 percent overall contribution within the entire

844 mNEN cohort were categorized under the “Filtered (<5%)” category. The proposed
845 etiology of the signatures is denoted below.

- 846 f) Relative frequency of the pyrimidine mutations (SNV) in their six categories.
- 847 g) Relative frequency of Doublet Base Substitution (DBS) categories.
- 848 h) Presence of chromothripsis; mNEN with chromothripsis are shown in pink.
- 849 i) Presence of kataegis; mNEN with kataegis are shown in red.
- 850 j) Status of homologous recombination deficiency (HRD), as determined by CHORD;
851 mNEN with *BRCA1/2*-associated HRD ($p \geq 0.5$) are shown in pink., otherwise colored
852 white.
- 853 k) Differentiation grade of the mNEN; NEC in red, NET in blue.
- 854 l) Primary localization of the mNEN.

855 **Figure 3 - Putative drivers and NEN-associated genes within the mNEN cohort as detected**
856 **by unbiased discovery (dN/dS, GISTIC2) and literature.**

857 Overview of putative drivers harboring coding mutations within at least three mNEN. We
858 show putative drivers as detected by dN/dS and/or GISTIC2 and supplemented this list with
859 additional NEN-associated drivers. mNEN and genes are sorted based on mutually-
860 exclusivity of the depicted putative drivers. Only GISTIC2 focal peaks with deep
861 amplifications and deletions are shown.

- 862 a) Number of genomic mutations per megabase over the entire genome (TMB); SNV,
863 InDel and MNV are depicted in blue, orange and salmon respectively. Threshold for
864 high-TMB (≥ 10) is shown by a horizontal salmon dashed line. Y-axis is shown in \log_{10} -
865 scale.
- 866 b) Mean genome-wide ploidy, ranging from 0 (red) to 4 (green; tetraploid). Diploidy is
867 shown in white.
- 868 c) Relative contribution of the COSMIC single-base substitution mutational signatures
869 (v3; $n = 67$). Signatures with less than 5 percent overall contribution within the entire
870 mNEN cohort were categorized under the “Filtered (<5%)” category. The proposed
871 etiology of the signatures is denoted below.
- 872 d) Overview of coding mutation(s) per mNEN, (light-)green or (light-)red backgrounds
873 depict copy-number aberrations whilst the inner square depicts the type of (coding)
874 mutation(s). The adjacent bar plots represent the relative proportions of mutational

875 categories (coding mutations (SNV, InDels and MNV), splicing mutations, SV, deep
876 gains (high-level amplifications resulting in many additional copies) and deep
877 deletions (high-level losses resulting in (near) homozygous losses) per gene. The
878 middle-outer barplot depicts the percentage of mNEC (in red) and mNET in blue
879 which harbored a mutation. In addition, dN/dS and/or GISTIC2 support are shown on
880 the outer-right bar plots for either the entire mNEN cohort or separate mNET/mNEC
881 analysis; GISTIC2 results are colored red if these genes were detected within a
882 recurrent focal deletion and green if detected within a recurrent focal gain.

- 883 e) Presence of chromothripsis; mNEN with chromothripsis are shown in pink.
- 884 f) Presence of kataegis; mNEN with kataegis are shown in red.
- 885 g) Status of homologous recombination deficiency (HRD), as determined by CHORD;
886 mNEN with *BRCA1/2*-associated HRD ($p \geq 0.5$) are shown in pink., otherwise colored
887 white.
- 888 h) Differentiation grade of the mNEN; mNEC in red, mNET in blue.
- 889 i) Primary localization of the mNEN.

890 **Figure 4 - Putative drivers and NEN-associated genes within the pancreas- and midgut-**
891 **derived mNET as detected by unbiased discovery (dN/dS, GISTIC2) and literature.**

892 Overview of putative drivers harboring coding mutations within at least two pancreas-
893 and/or midgut-derived mNET. We show putative drivers as detected by subgroup-specific
894 dN/dS and/or GISTIC2 and supplemented this list with additional NEN-associated drivers.
895 mNET and genes are sorted based on mutually-exclusivity of the depicted putative drivers.
896 Same layout as figure 3, except the adjacent middle-outer bar (in **d**) depicts the percentage
897 of pancreas-derived m(NET) in green and midgut-derived mNET in blue. In addition, **e**)
898 represent chromosomal arm-aberrations on chr18_{p/q} as detected by GISTIC2.

899 **Figure 5 - Clinically-actionable somatic alterations observed within mNEN.**

- 900 a) Overview of distinct mNEN harboring current clinically-actionable alterations for on-
901 and off-label NEN therapies. The highest NEN-therapy option (ranked as on-label
902 NEN subtype, on-label NEN, off-label for NEN, off-label for other cancer types but
903 currently-available and drugs in development) per distinct mNEN is shown.
- 904 b) mNEN harboring current clinically-actionable alterations, per gene. The highest NET-
905 therapy option per mNEN and gene is shown. Bottom track represents the

906 categorized primary localization of the mNEN whilst the right-hand side figure shown
907 the number of samples harboring a somatic alteration within the given gene and the
908 proposed level of therapy.

909 **Supplemental data**

910 **Supp. Figure 1 - Overview of participating Dutch centers in the CPCT-02 mNEN cohort.**

- 911 a) Absolute frequency of distinct included patients in the CPCT-02 mNEN cohort per
912 participating center within the Netherlands, shown with their geographical position.
913 b) Absolute and relative frequencies of distinct included patients in the CPCT-02 mNEN
914 cohort per participating center within the Netherlands.

915 **Supp. Figure 2 - Overview of sequencing characteristics and selected biopsies.**

- 916 a) Boxplot with individual data points of the estimated (*in silico*) tumor cell
917 percentages based on the whole genome sequencing data with observed median
918 displayed.
919 b) Boxplot with individual data points of the mean read-coverages (WGS) of the
920 peripheral blood (reference; blue) and biopsy tissues (red) with observed median
921 per variable displayed.
922 c) Age distribution stratified by gender of the mNEN cohort with observed median
923 per variable displayed in a boxplot with individual data points.
924 d) Generalized location of the biopsy with the relative frequency shown between
925 brackets.

926 **Supp. Figure 3 - Overview of mutational landscape, categorized per differentiation grade.**

- 927 a) Number of SNV (gray), InDels (green), MNV (salmon) per whole-genome sequenced
928 sample over three resolutions; genome-wide, within intragenic regions and within
929 coding regions with observed median per variable displayed. Data is categorized on
930 mNEC / mNET status.
931 b) Type of genome-wide SNVs. Transition (Ti) and transversion (Tv), with a special
932 attention for C to T (Ti) in CpG context, are indicated per sample with observed
933 median per variable displayed. Data is categorized on mNEC / mNET status.
934 c) Mean genome-wide tumor ploidy based on all autosomal chromosomes with
935 observed median displayed. Data is categorized on mNEC / mNET status.
936 d) Frequency of Tandem Duplications, Insertions, Inversions, Deletions and
937 interchromosomal translocations are indicated per sample with observed median
938 per variable displayed. Data is categorized on mNEC / mNET status.

- 939 e) Mutational consequences of genomic variants overlapping genes using Ensembl
940 Variant Effect Predictor (VEP). Data is categorized on mNEC / mNET status.
- 941 f) Genome-wide ratio of transitions (Ti) over transversion (Tv) with observed median
942 displayed. Data is categorized on mNEC / mNET status.

943 **Supp. Figure 4 - Overview of the distribution of somatically-acquired structural variants.**

944 Overview of the genomic sizes and numbers of structural variants present in the mNEN
945 cohort. Samples are sorted based on primary localization and decreasing number of total
946 observed structural variants over all categories (deletions, tandem duplications, inversions,
947 translocations and insertions).

- 948 a) Track displays boxplots representing the genomic width of deletions; Y-axis is in
949 \log_{10} -scale. Lower track displays the total number of observed deletions.
- 950 b) Track displays boxplots representing the genomic width of tandem duplications; Y-
951 axis is in \log_{10} -scale. Lower track displays the total number of observed tandem
952 duplications.
- 953 c) Track displays boxplots representing the genomic width of inversions; Y-axis is in
954 \log_{10} -scale. Lower track displays the total number of observed inversions.
- 955 d) Total number of observed translocations.
- 956 e) Total number of observed insertions.
- 957 f) Presence of chromothripsis, kataegis and/or predicted HRD (CHORD). Bottom track
958 displays differentiation grade (NEC/NET) and primary localization of mNEN.

959

960 **Supp. Figure 5 - Observed kataegis events within the mNET cohort.**

- 961 a) Number of observed kataegis foci in the mNEN cohort (found in 6 distinct samples,
962 blue bars) and the respective cumulative genomic width of all observed kataegis foci
963 per sample (right y-axis; black points).
- 964 b) Relative frequency of SNV categories found in all observed kataegis foci per sample.
- 965 c) Relative frequency of SNV in observed kataegis foci with APOBEC-related TpCpW
966 mutational context. W stands for T or A changes.
- 967 d) Genome-wide relative contribution to mutational signatures (COSMIC v3) for the
968 respective mNET sample.

- 969 e) Representation of a single kataegis foci on chromosome 8 within a single respective
970 sample (highlighted with * in a). SNV (colored on pyrimidine mutations) are shown
971 with relative genomic distances (in \log_{10}) to neighboring SNV. Observed kataegis
972 focus on chromosome 8 is highlighted with a transparent red background.
- 973 f) Absolute mutational contribution of APOBEC COSMIC (v3) signatures (2 & 13) for
974 samples without ($n = 80$) and with observed kataegis foci ($n = 6$). Statistical
975 significance was tested with Wilcoxon rank-sum test and is denoted with * ≤ 0.05 , **
976 ≤ 0.01 and *** ≤ 0.001 .

977 **Supp. Figure 6 - Genomic overview of mNEN displaying chromothripsis-like events.**

978 Genomic representations of the chromothripsis-harboring mNEN ($n = 6$). The outer track
979 displays the genomic ideogram, the second-outer track displays copy number profiles
980 (amplification in light green; deep amplification beyond sample-specific threshold (GISTIC2)
981 in dark green, deletions in blue; deep deletions beyond sample-specific threshold (GISTIC2)
982 in dark blue). The third track displays TC%-corrected lower allele-frequency (LAF) values of
983 individual copy number segments (LAF ≤ 0.33 in pink; LAF ≥ 0.33 in black). The fourth track
984 displays the number of mutations per 5 Mbp, ranging from 0 to 60+; bins with ≥ 20
985 mutations are highlighted in blue. The fifth track highlights the regions harboring
986 chromothripsis in a red line. The innermost track displays the breakpoints of the structural
987 variants; interchromosomal translocations in dark blue, deletions in gray, insertions in
988 yellow, inversion in light blue and tandem duplications in red. Samples are colored per NEC
989 (in red) and NET (in blue) status.

990 **Supp. Figure 7 - *de novo* mutational signatures assessment on mNEN.**

991 Assessment and comparison of extracted *de novo* single base substitution mutational
992 signatures ($n = 7$; Sig. A - I) using non-negative matrix factorization (NMF) within the mNEN
993 cohort against the known COSMIC (v3; $n = 67$) signatures.

- 994 a) Overview of extracted *de novo* single base substitution mutational signatures ($n = 7$;
995 Sig. A - I; upper track) vs. COSMIC signatures (v3; $n = 67$; lower track), per mNEN.
996 mNEN are sorted based on unsupervised clustering (Ward.D; Euclidean distance;
997 distances plotted in \log_{10} -scale) of the relative contribution of the nine *de novo*
998 mutational signatures.

- 999 b) Cosine similarity of the *de novo* mutational signatures against the known COSMIC v3
1000 signatures ($n = 67$).
1001 c) Trinucleotide mutational contexts of the nine extracted *de novo* signatures.
1002 d) NMF quality metrics using between two to fifteen ranks over 1000 iterations.

1003 **Supp. Figure 8 - Copy-number overview of mNEN cohort and subpopulations with re-**
1004 **occurring and focal amplifications and deletion highlighted (GISTIC2) and unbiased driver**
1005 **gene analysis.**

1006 Circosplots with ideogram of recurrent copy-number aberrations as detected by GISTIC2 per
1007 sub-population (as shown above each circosplot). G-scores are depicted on the y-axis.
1008 Regions with amplifications (G-score > 0) are depicted in green and deletions (G-score < 0) in
1009 blue. Regions with significant (and recurring) copy-number aberrations ($q \leq 0.1$) are denoted
1010 with a darker shade of green or blue, respective of amplification or deletion. Per region, the
1011 foci of maximal amplification or deletion (focal peaks; $q \leq 0.1$) are denoted in the inner
1012 track; the peak identifiers with associated genes are also denoted and presented in
1013 supplementary table 1.

1014 **Supp. Figure 9 - Genomic characteristics per differentiation grade (NEC/NET) and primary**
1015 **localization within mNET.**

- 1016 a) Number of SNV, InDels, MNV and SV per whole-genome mNEN with observed
1017 median per variable displayed. Data is categorized on mNEC and distinct mNET
1018 subgroups based on primary localization.
1019 b) Tumor mutational burdens (genome-wide; \log_{10}), with observed median per variable
1020 displayed. Data is categorized on mNEC and distinct mNET subgroups based on
1021 primary localization.
1022 c) Mean genome-wide ploidy, with observed median per variable displayed. Data is
1023 categorized on mNEC and distinct mNET subgroups based on primary localization.
1024 d) Number of genes harboring somatic coding mutations, with observed median per
1025 variable displayed. Data is categorized on mNEC and distinct mNET subgroups based
1026 on primary localization.
1027 e) Mutational enrichment of mutant genes (mutations and copy-number alterations)
1028 and large-scale events (kataegis and chromothripsis) between our three major
1029 subgroups; mNEC, pancreas- and midgut-derived mNET. Statistical significance was

1030 tested using a one-sided Fisher's Exact Test with BH correction; significance is
1031 denoted by *** ($q \leq 0.001$), ** ($q \leq 0.01$), * ($q \leq 0.05$) and . ($q \leq 0.1$).

1032

1033 **Supp. Figure 10 - Copy-number aberrations of chromosomal arms per differentiation**
1034 **grade (NEC/NET) and primary localization within mNET.**

1035 a) Unsupervised clustering (Euclidean distances, Ward.D2 method) of the mNET
1036 samples based on the categorization of chromosomal arm copy-number aberrations
1037 (based on GISTIC2 value per arm). Top color-bars depict the differentiation grade of
1038 the mNEN (mNEC in red, mNET in blue) and the primary localization.

1039 b) Overview of the relative frequency of samples with amplifications (green) and losses
1040 (red) per arm within the given subgroup. Statistically significant ($q \leq 0.05$) arm-level
1041 copy-number aberrations are depicted with an asterisk whilst the non-significant
1042 events are shown as transparent.

1043 **Supp. Table 1 - Overview of included patients and data presented in figures.**

1044 Overview of all data presented and quantified in this manuscript.

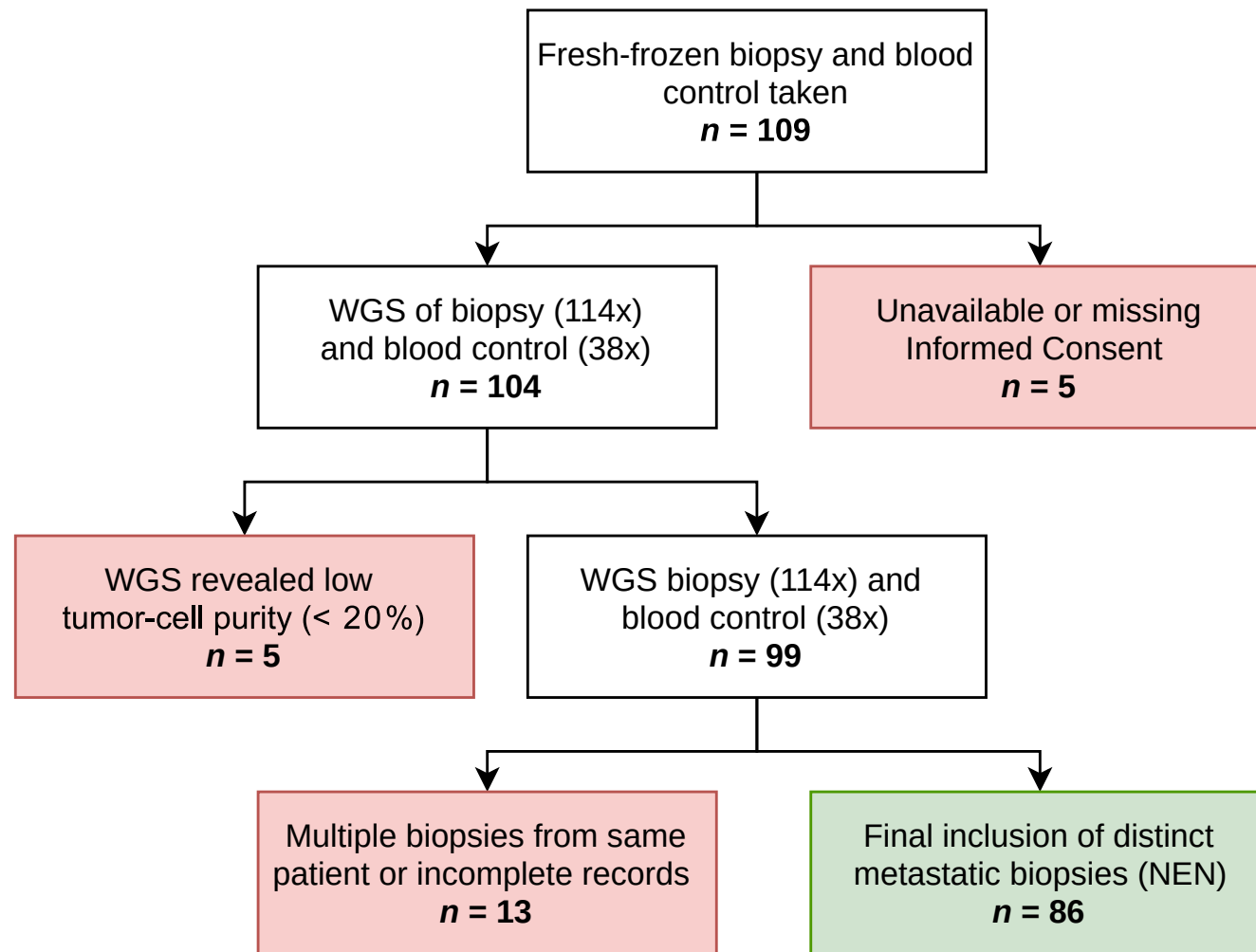
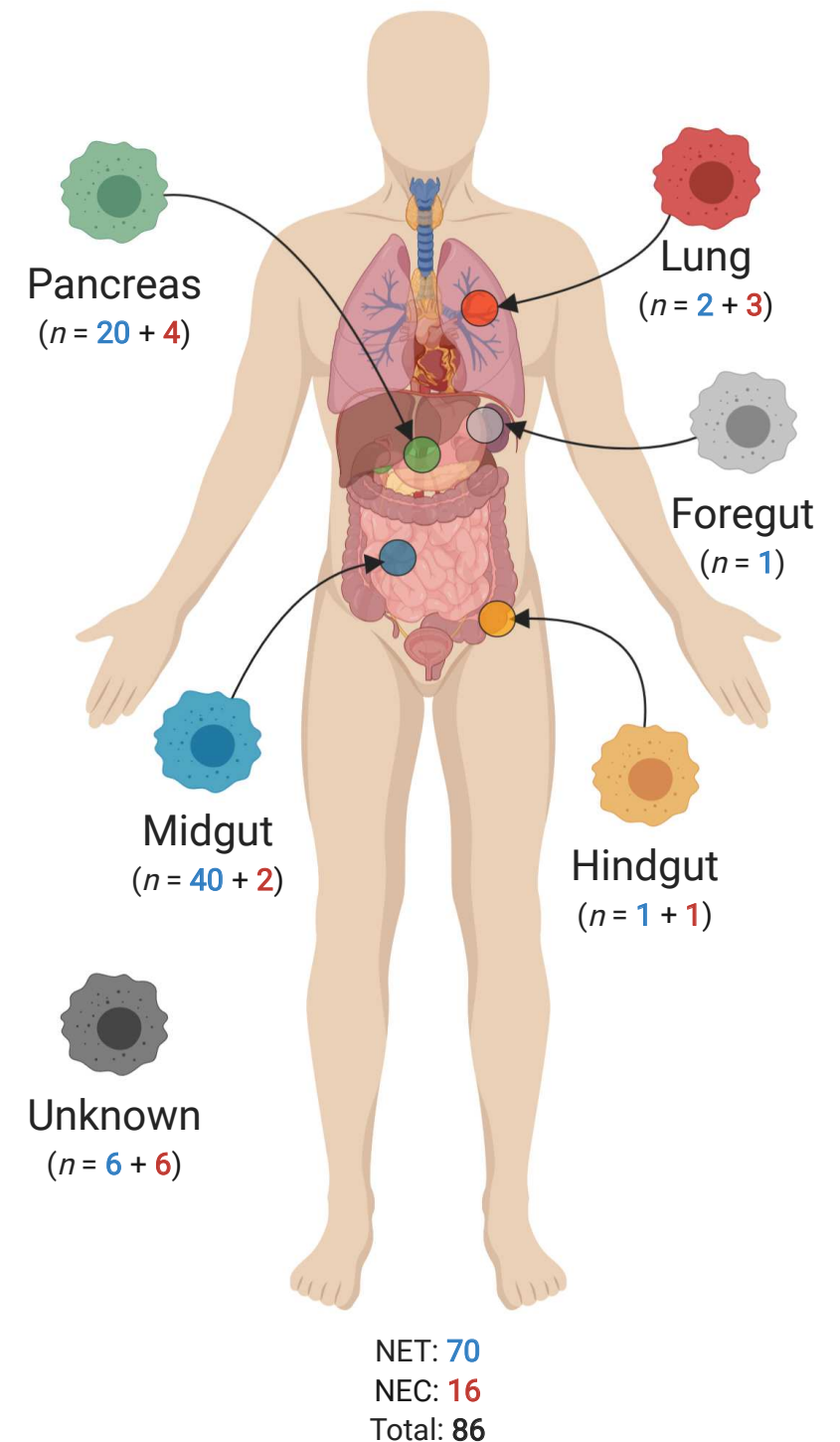
a**b**

Figure 1 - Overview of patient inclusion and sub-classification of biopsies.

a) Flowchart of patient inclusion. From the CPCT-02 cohort, single biopsies from 86 distinct patients with metastatic neuroendocrine neoplasms (mNEN) were selected. From the total pool of available whole-genome sequenced mNET samples. If multiple derived mNET biopsies from the same patient were available, we selected the mNET biopsy with the highest tumor cell purity.

b) Subclassification of mNEN based on primary localization. The 86 mNEN were subclassified, based on their primary localization, into six major categories; Foregut, Hindgut, Lung, Pancreas and Midgut; whilst samples with indeterminable localization were categorized as Unknown. The number of mNET (in blue) and mNEC (in red) are shown per category.

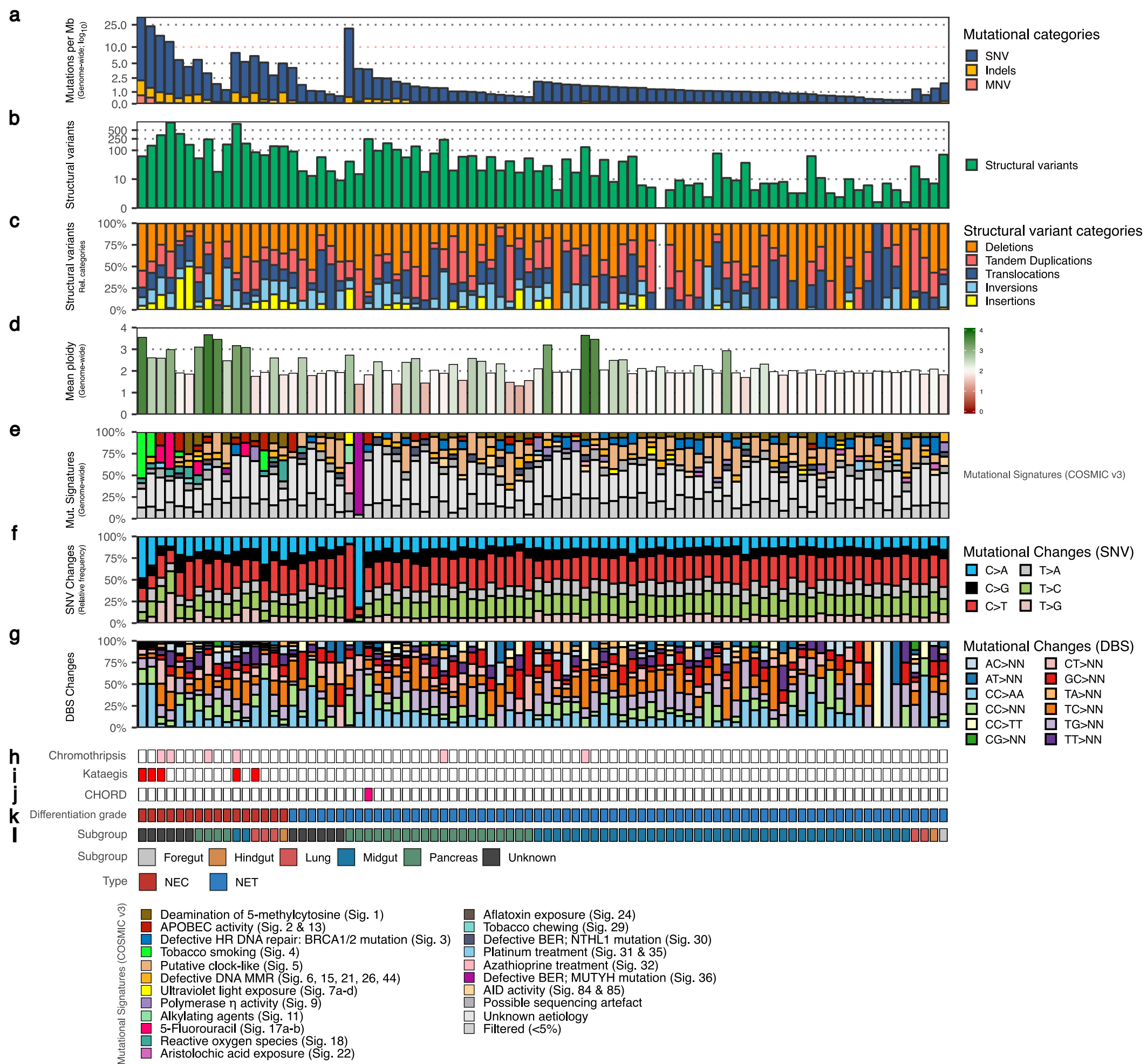


Figure 2 - Landscape of large-scale genomic alterations detected in mNEN, ordered by differentiation grade (NEC / NET) and primary localization.

Overview of genome-wide characteristics of the mNEN cohort ordered by mNEC / mNET and primary localization on decreasing median tumor mutational burden. For each mNEN ($n = 86$), the following tracks are shown:

a) Number of genomic mutations per megabase over the entire genome (TMB); SNV, InDel and MNV are depicted in blue, orange and salmon respectively. Threshold for high-TMB (≥ 10) is shown by a horizontal red dotted line. Y-axis is shown in log10-scale.

b) Total number of structural variants including deletions, tandem duplications, translocations, inversions and insertions as detected by GRIDSS. Y-axis is shown in log10-scale.

c) Relative frequency of each of the structural variant categories; deletions in orange, tandem duplications in red, translocations in blue, inversions in light-blue and insertions in yellow.

d) Mean genome-wide ploidy, ranging from 0 (red) to 4 (green; tetraploid). Common diploid status is shown in white.

e) Relative contribution of the COSMIC single-base substitution mutational signatures (v3; $n = 67$). Signatures with less than 5 percent overall contribution within the entire mNEN cohort were categorized under the “Filtered (<5%)” category. The proposed etiology of the signatures is denoted below.

f) Relative frequency of the pyrimidine mutations (SNV) in their six categories.

g) Relative frequency of Doublet Base Substitution (DBS) categories.

h) Presence of chromothripsis; mNEN with chromothripsis are shown in pink.

i) Presence of kataegis; mNEN with kataegis are shown in red.

j) Status of homologous recombination deficiency (HRD), as determined by CHORD; mNEN with BRCA1/2-associated HRD ($p \geq 0.5$) are shown in pink., otherwise colored white.

k) Differentiation grade of the mNEN; NEC in red, NET in blue.

l) Primary localization of the mNEN.

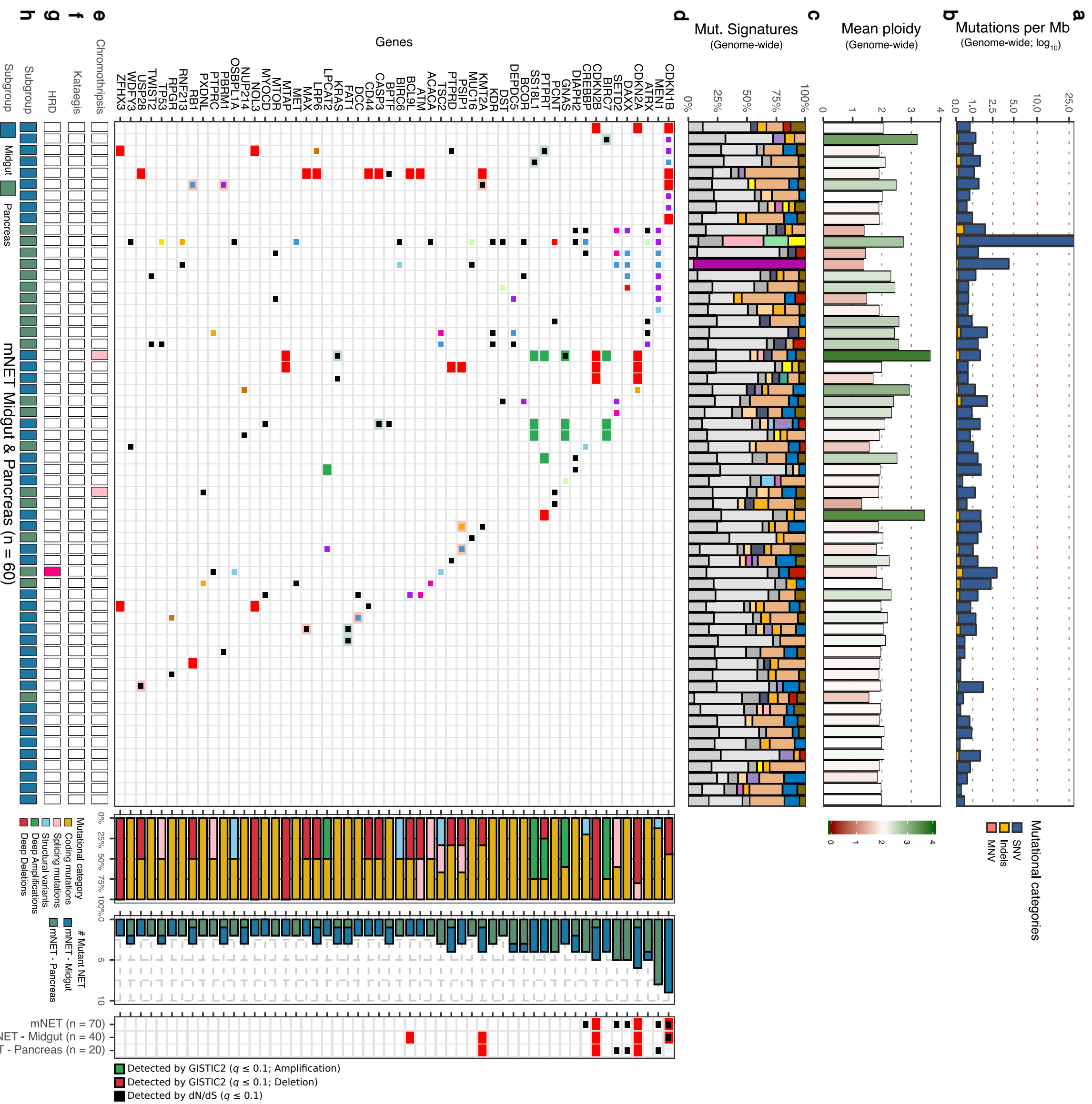


Figure 4 - Putative drivers and NEN-associated genes within the pancreas- and midgut-derived mNET as detected by unbiased discovery (dn/ds, GISTIC2) and literature.

Overview of putative drivers harboring coding mutations within at least two pancreas- and/or midgut-derived mNET. We show putative drivers as detected by subgroup-specific dn/ds and/or GISTIC2 and supplemented this list with additional NEN-associated drivers. mNET and genes are sorted based on mutually-exclusivity of the depicted putative drivers. Same layout as figure 3, except the adjacent middle-outer bar (in **d**) depicts the percentage of pancreas-derived m(NET) in green and midgut-derived mNET in blue. In addition, **e**) represent chromosomal arm-aberrations on chr18p/q as detected by GISTIC2.

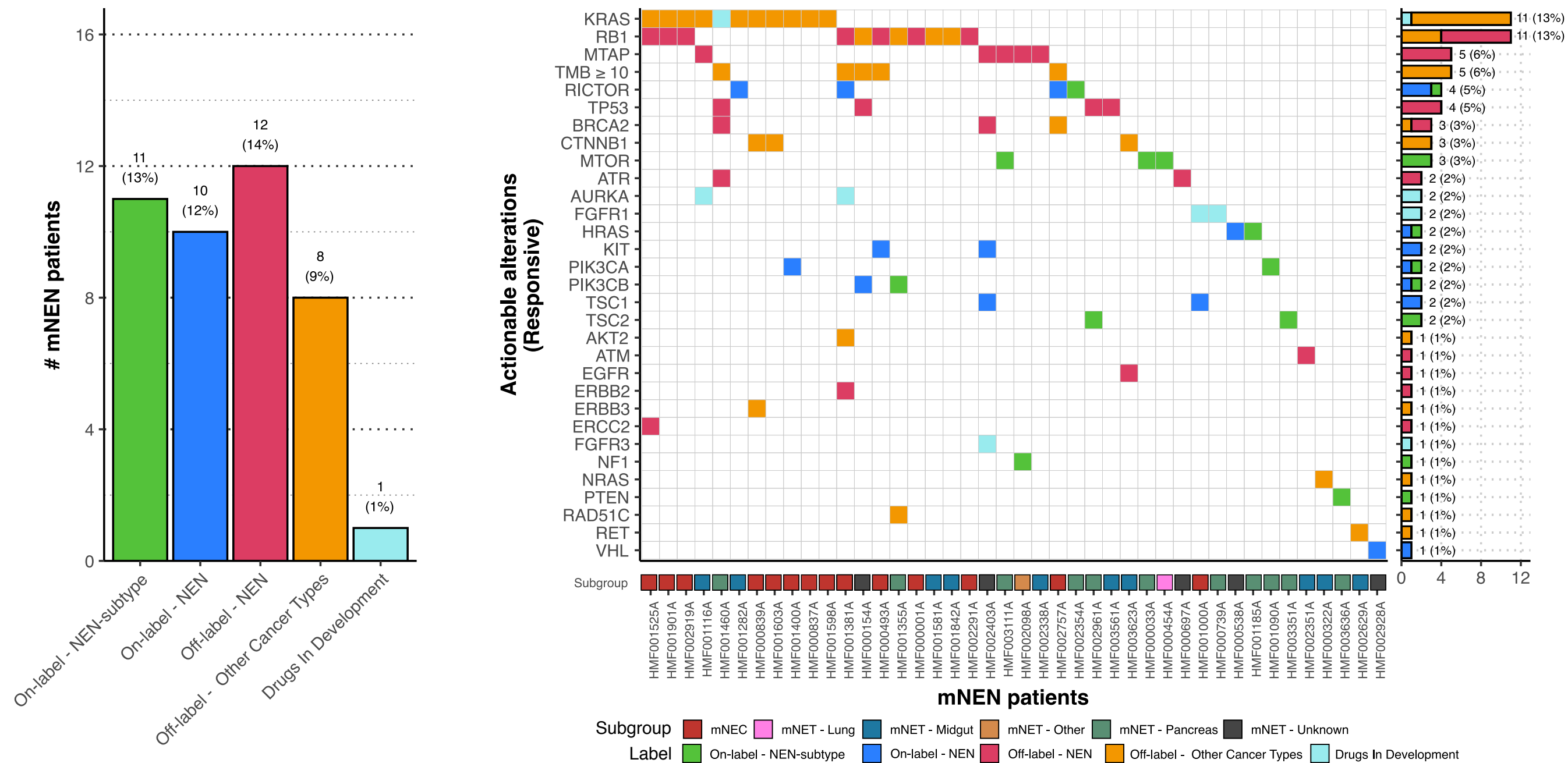
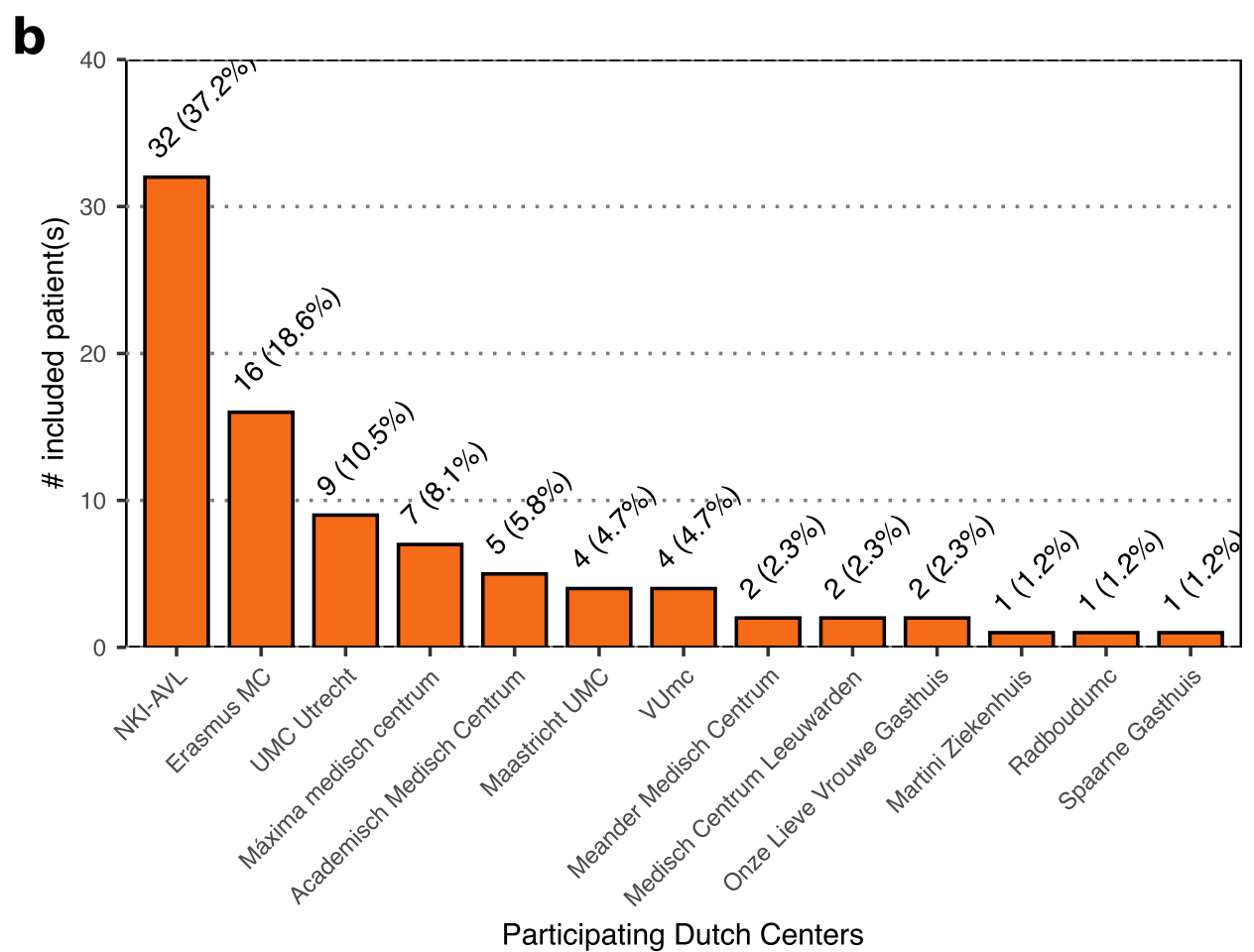


Figure 5 - Clinically-actionable somatic alterations observed within mNEN.

a) Overview of distinct mNEN harboring current clinically-actionable alterations for on- and off-label NEN therapies. The highest NEN-therapy option (ranked as on-label NEN subtype, on-label NEN, off-label for NEN, off-label for other cancer types but currently-available and drugs in development) per distinct mNEN is shown.

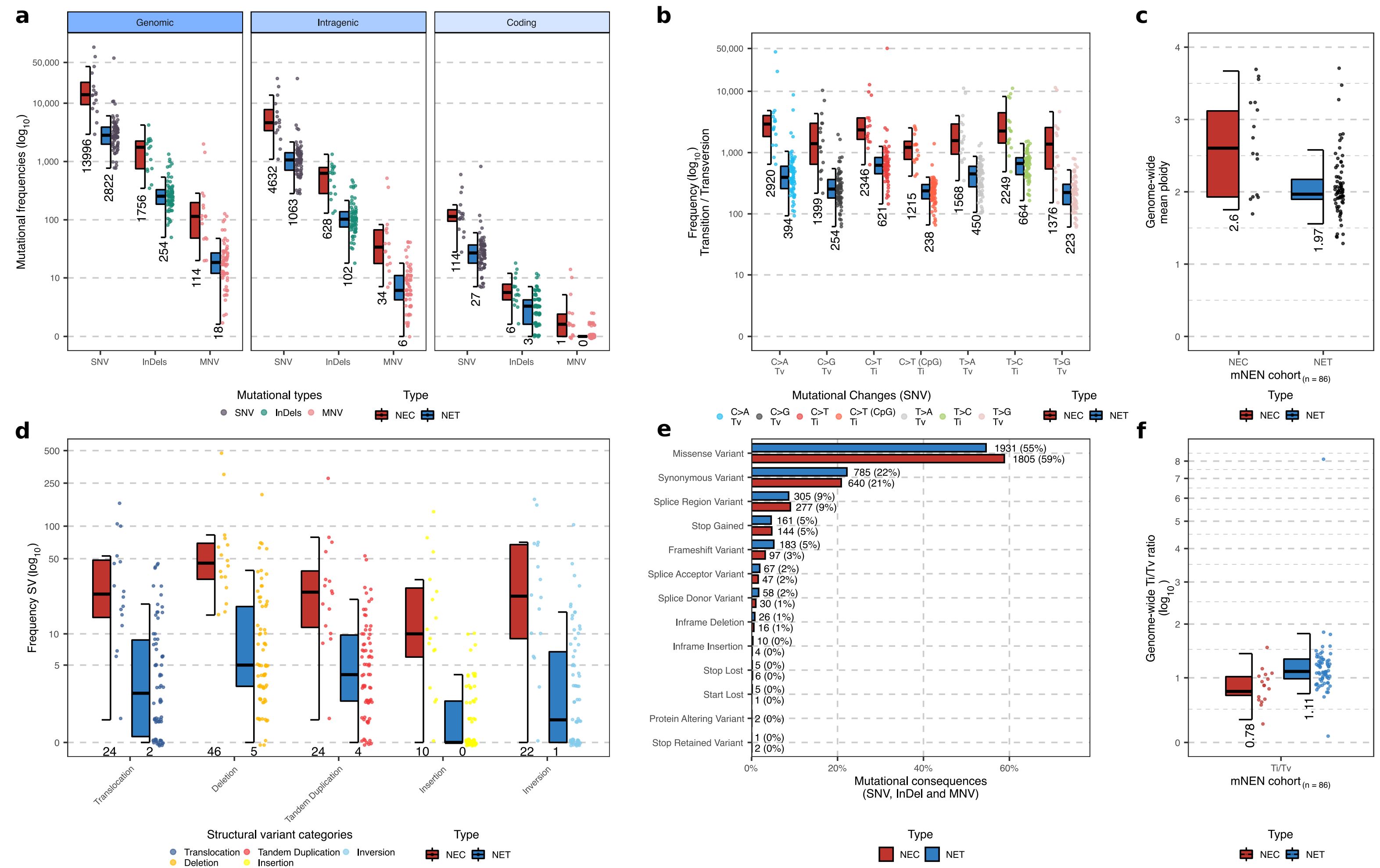
b) mNEN harboring current clinically-actionable alterations, per gene. The highest NET-therapy option per mNEN and gene is shown. Bottom track represents the categorized primary localization of the mNEN whilst the right-hand side figure shown the number of samples harboring a somatic alteration within the given gene and the proposed level of therapy.



Supp. Figure 1 - Overview of participating Dutch centers in the CPCT-02 mNEN cohort.

a) Absolute frequency of distinct included patients in the CPCT-02 mNEN cohort per participating center within the Netherlands, shown with their geographical position.

b) Absolute and relative frequencies of distinct included patients in the CPCT-02 mNEN cohort per participating center within the Netherlands.



Supp. Figure 3 - Overview of mutational landscape, categorized per differentiation grade.

a) Number of SNV (gray), InDels (green), MNV (salmon) per whole-genome sequenced sample over three resolutions; genome-wide, within intragenic regions and within coding regions with observed median per variable displayed. Data is categorized on mNEC / mNET status.

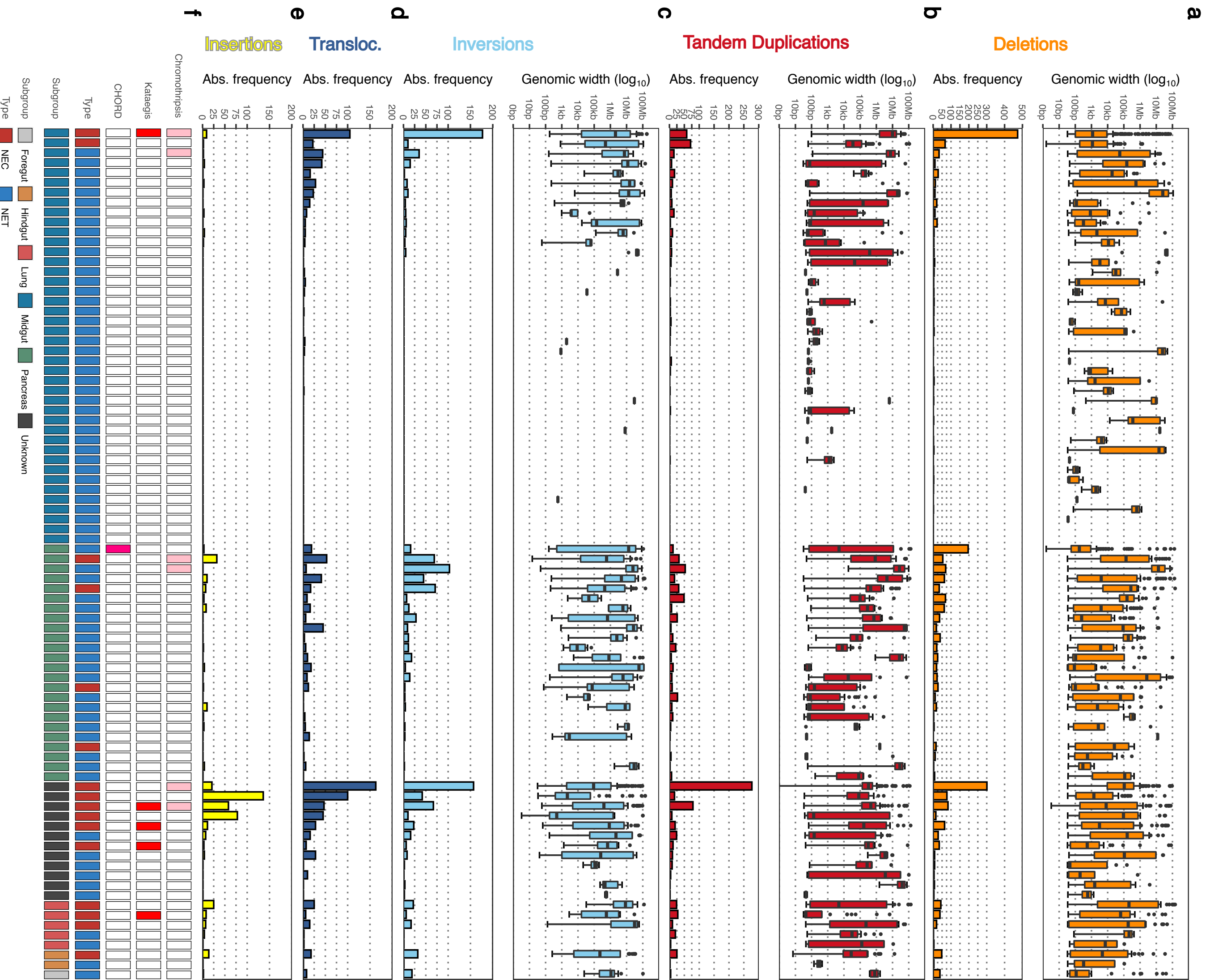
b) Type of genome-wide SNVs. Transition (Ti) and transversion (Tv), with a special attention for C to T (Ti) in CpG context, are indicated per sample with observed median per variable displayed. Data is categorized on mNEC / mNET status.

c) Mean genome-wide tumor ploidy based on all autosomal chromosomes with observed median displayed. Data is categorized on mNEC / mNET status.

d) Frequency of Tandem Duplications, Insertions, Inversions, Deletions and interchromosomal translocations are indicated per sample with observed median per variable displayed. Data is categorized on mNEC / mNET status.

e) Mutational consequences of genomic variants overlapping genes using Ensembl Variant Effect Predictor (VEP). Data is categorized on mNEC / mNET status.

f) Genome-wide ratio of transitions (Ti) over transversion (Tv) with observed median displayed. Data is categorized on mNEC / mNET status.



Supp. Figure 4 - Overview of the distribution of somatically-acquired structural variants.

Overview of the genomic sizes and numbers of structural variants present in the mNEN cohort. Samples are sorted based on primary localization and decreasing number of total observed structural variants over all categories (deletions, tandem duplications, inversions, translocations and insertions).

a) Track displays boxplots representing the genomic width of deletions; Y-axis is in \log_{10} -scale. Lower track displays the total number of observed deletions.

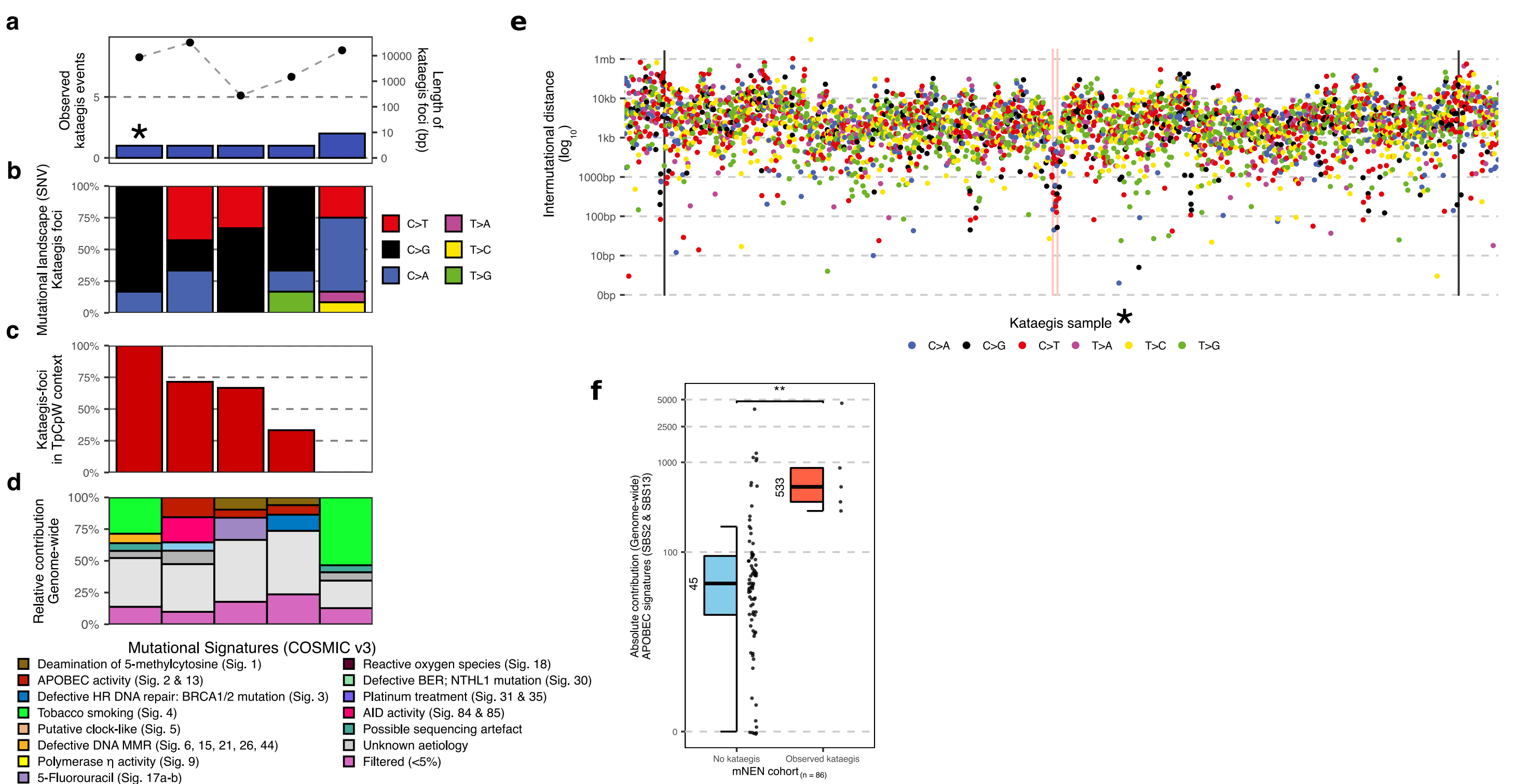
b) Track displays boxplots representing the genomic width of tandem duplications; Y-axis is in \log_{10} -scale. Lower track displays the total number of observed tandem duplications.

c) Track displays boxplots representing the genomic width of inversions; Y-axis is in \log_{10} -scale. Lower track displays the total number of observed inversions.

d) Total number of observed translocations.

e) Total number of observed insertions.

f) Presence of chromothripsis, kataegis and/or predicted HRD (CHORD). Bottom track displays differentiation grade (NEC/NET) and primary localization of mNEN.



Supp. Figure 5 - Observed kataegis events within the mNET cohort.

a) Number of observed kataegis foci in the mNET cohort (found in 6 distinct samples, blue bars) and the respective cumulative genomic width of all observed kataegis foci per sample (right y-axis; black points).

b) Relative frequency of SNV categories found in all observed kataegis foci per sample.

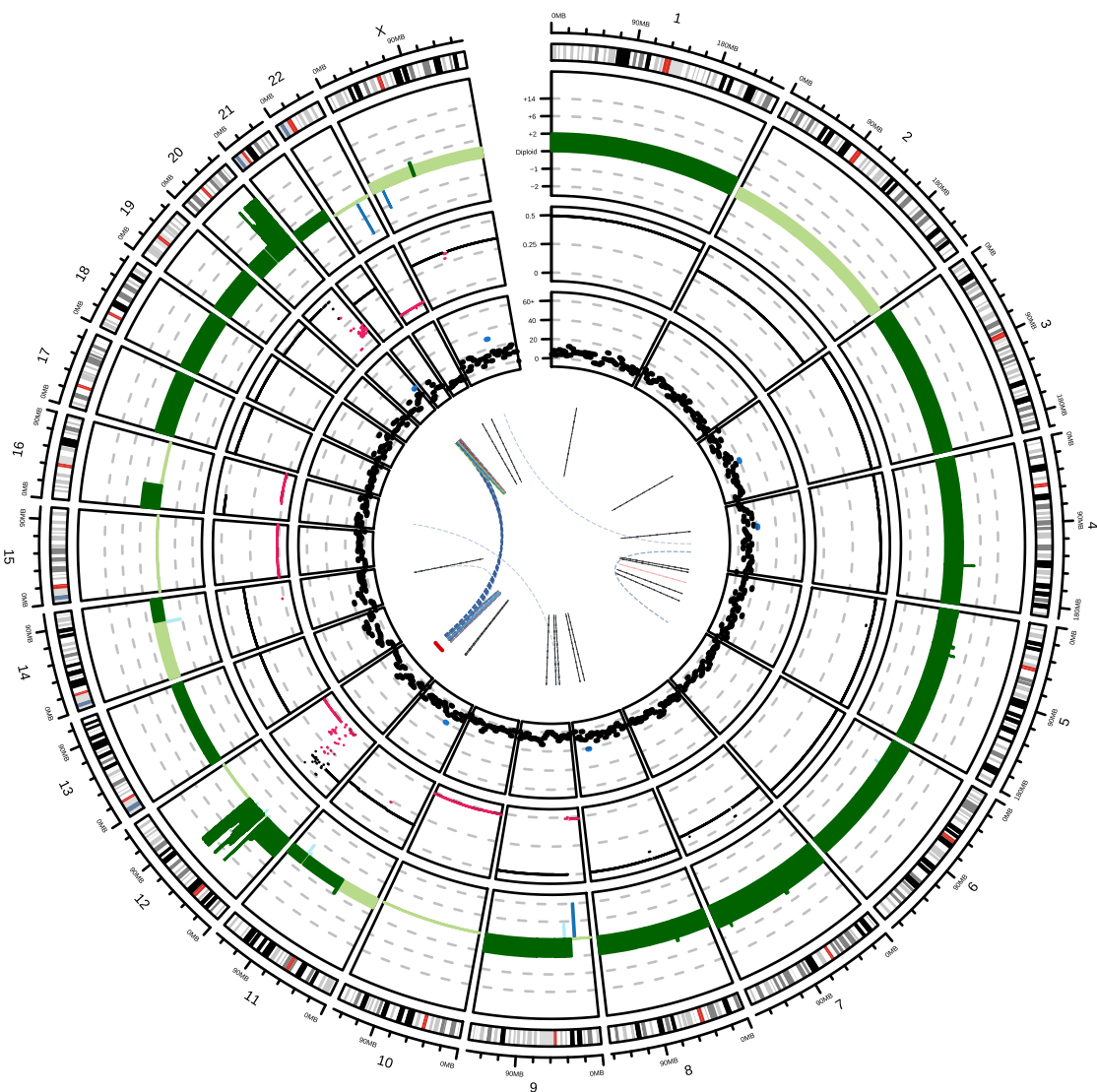
c) Relative frequency of SNV in observed kataegis foci with APOBEC-related TpCpW mutational context. W stands for T or A changes.

d) Genome-wide relative contribution to mutational signatures (COSMIC v3) for the respective mNET sample.

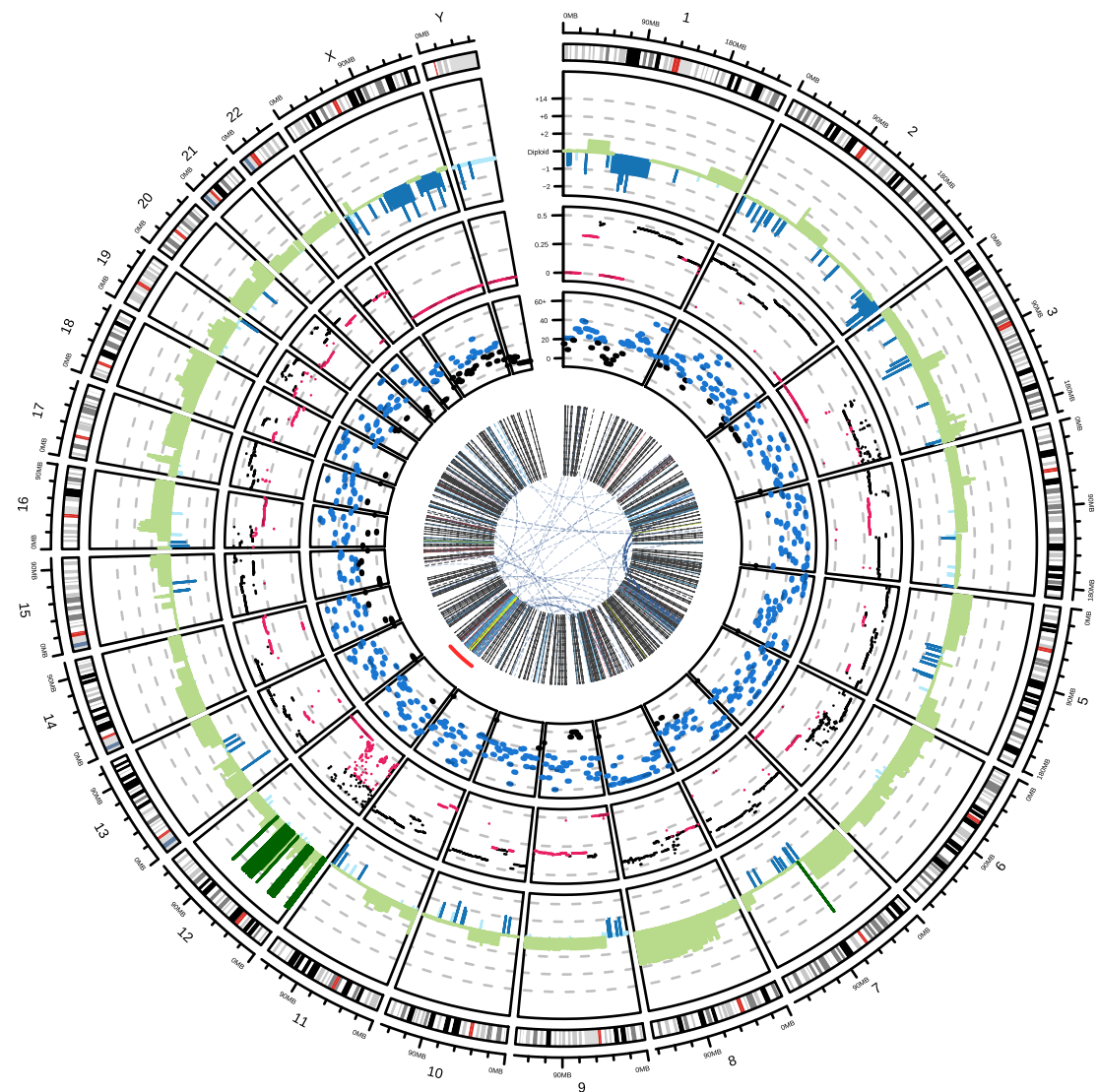
e) Representation of a single kataegis foci on chromosome 8 within a single respective sample (highlighted with * in **a**). SNV (colored on pyrimidine mutations) are shown with relative genomic distances (in \log_{10}) to neighboring SNV. Observed kataegis focus on chromosome 8 is highlighted with a transparent red background.

f) Absolute mutational contribution of APOBEC COSMIC (v3) signatures (2 & 13) for samples without ($n = 80$) and with observed kataegis foci ($n = 6$). Statistical significance was tested with Wilcoxon rank-sum test and is denoted with * ≤ 0.05 , ** ≤ 0.01 and *** ≤ 0.001 .

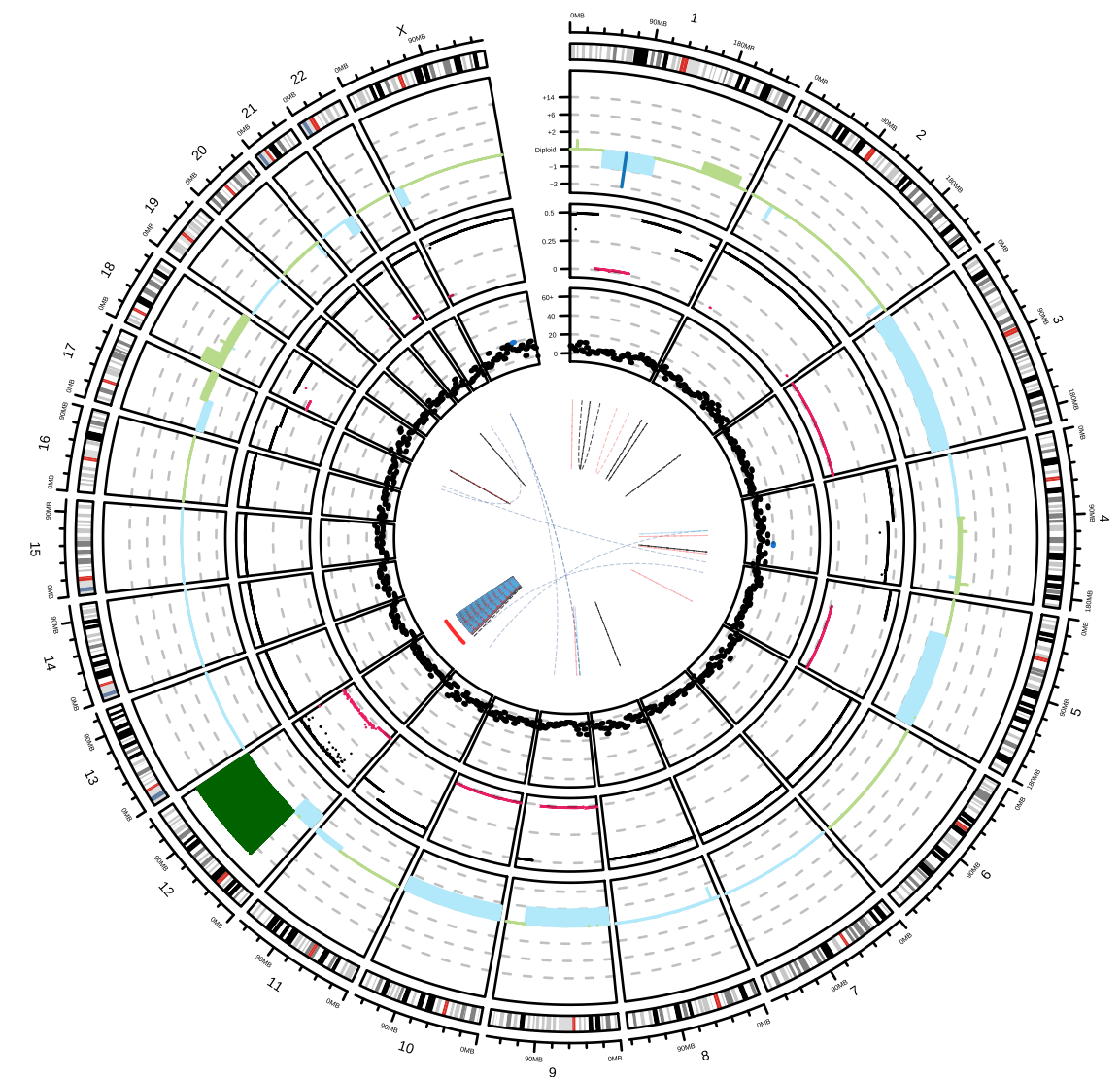
HMF001116A



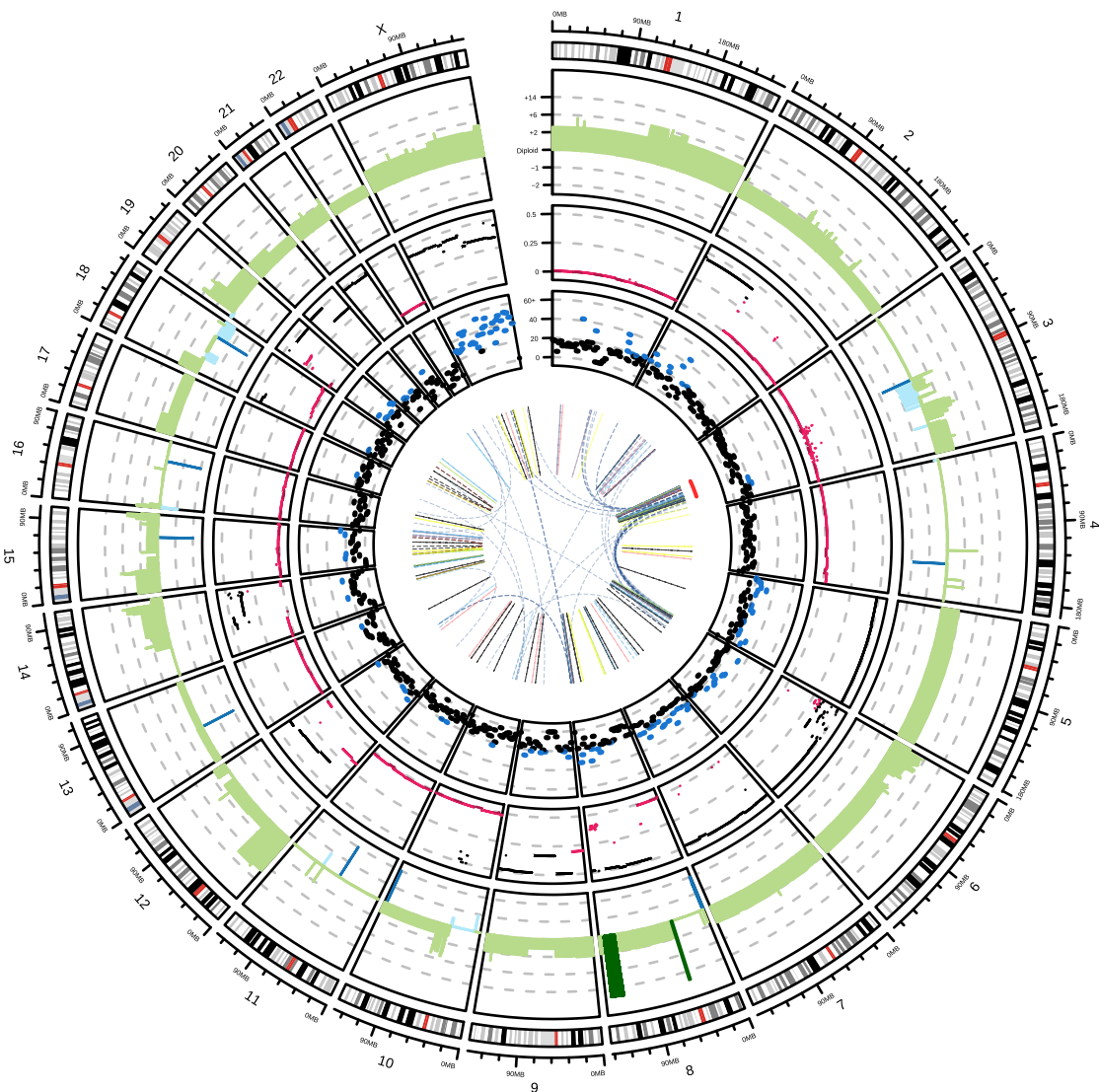
HMF000839A



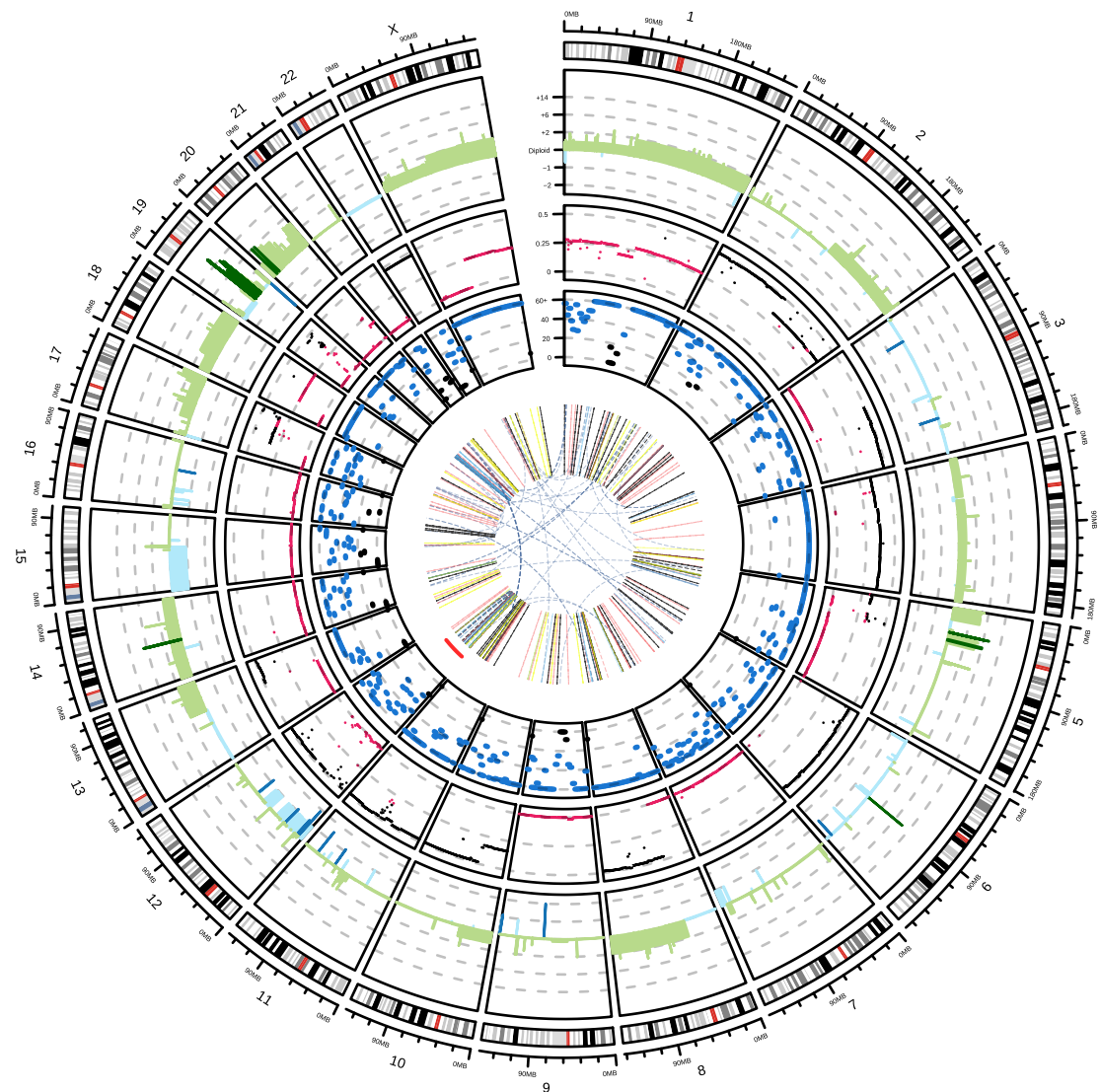
HMF003590A



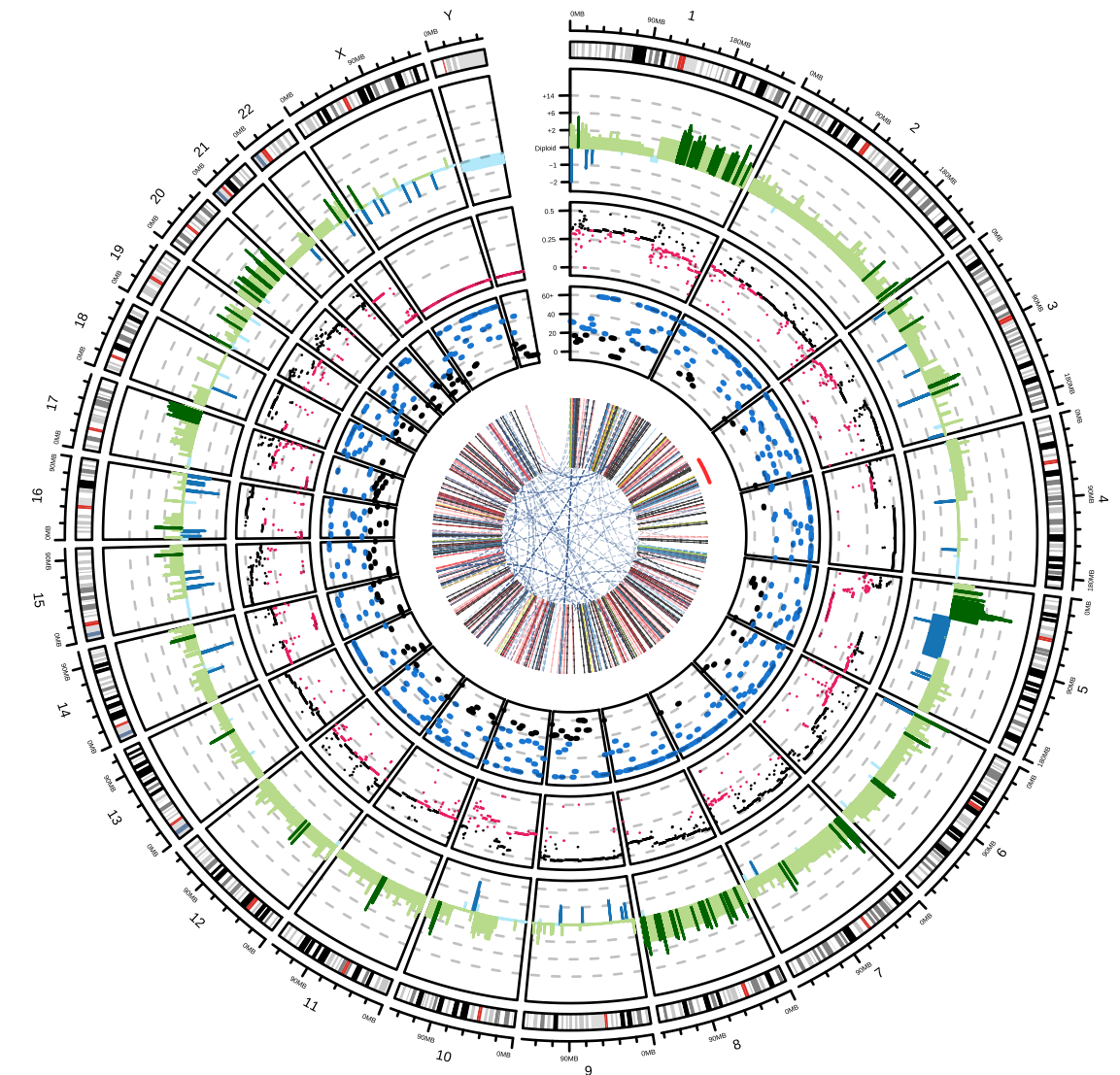
HMF001901A



HMF001381A

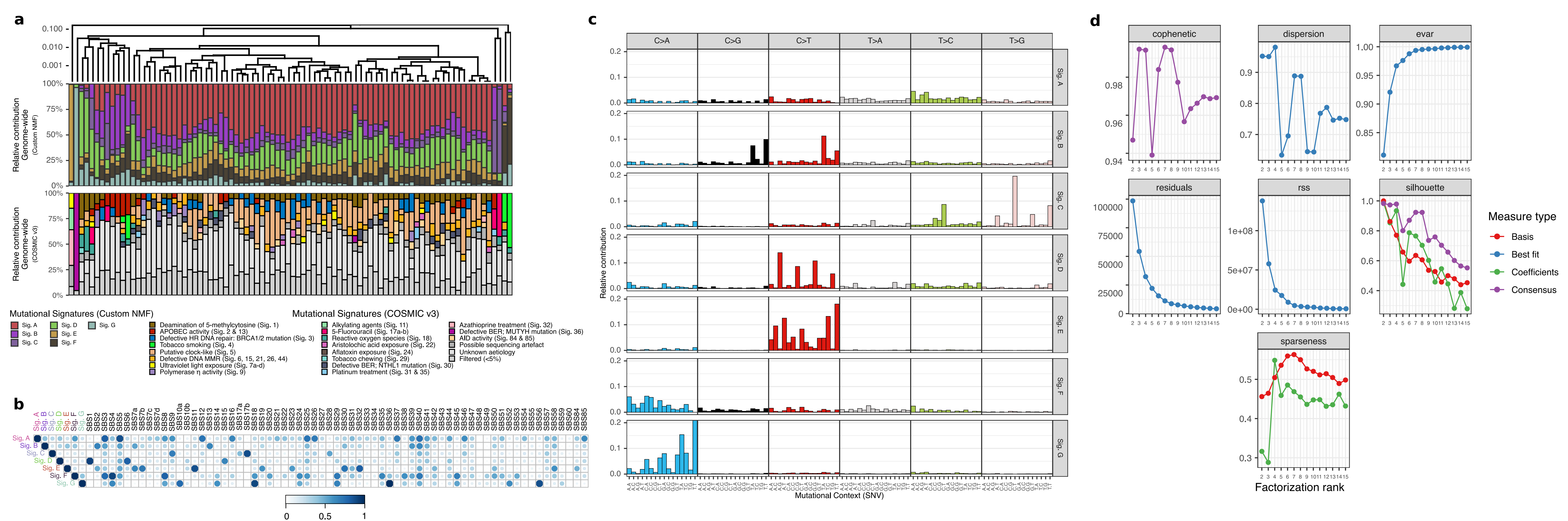


HMF002757A



Supp. Figure 6 - Genomic overview of mNEN displaying chromothripsis-like events.

Genomic representations of the chromothripsis-harboring mNEN ($n = 6$). The outer track displays the genomic ideogram, the second-outer track displays copy number profiles (amplification in light green; deep amplification beyond sample-specific threshold (GISTIC2) in dark green, deletions in blue; deep deletions beyond sample-specific threshold (GISTIC2) in dark blue). The third track displays TC%-corrected lower allele-frequency (LAF) values of individual copy number segments (LAF ≤ 0.33 in pink; LAF ≥ 0.33 in black). The fourth track displays the number of mutations per 5 Mbp, ranging from 0 to 60+; bins with ≥ 20 mutations are highlighted in blue. The fifth track highlights the regions harboring chromothripsis in a red line. The innermost track displays the breakpoints of the structural variants; interchromosomal translocations in dark blue, deletions in gray, insertions in yellow, inversion in light blue and tandem duplications in red. Samples are colored per NEC (in red) and NET (in blue) status.



Supp. Figure 7 - de novo mutational signatures assessment on mNEN.

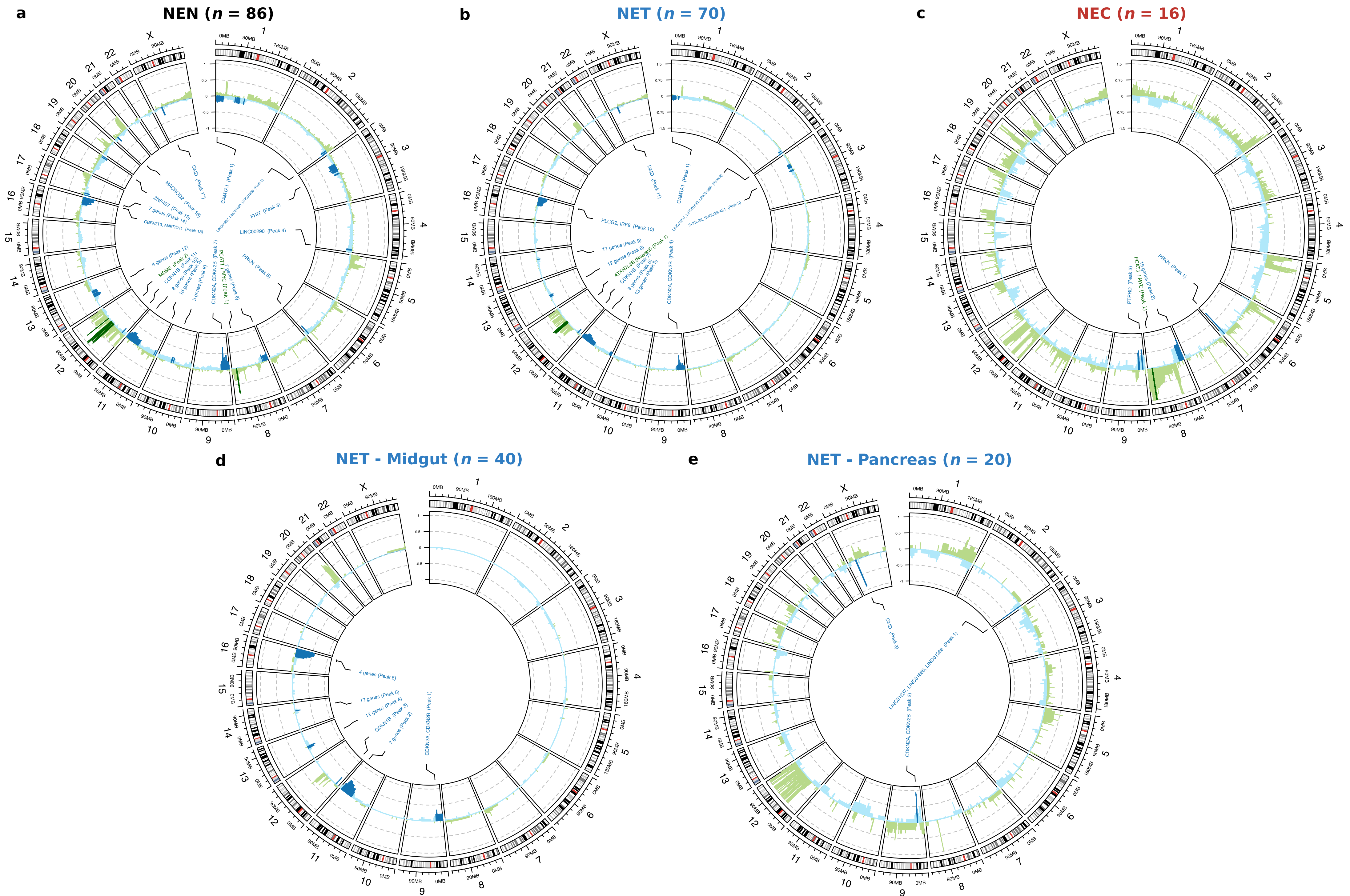
Assessment and comparison of extracted de novo single base substitution mutational signatures ($n = 7$; Sig. A - I) using non-negative matrix factorization (NMF) within the mNEN cohort against the known COSMIC (v3; $n = 67$) signatures.

a) Overview of extracted de novo single base substitution mutational signatures ($n = 7$; Sig. A - I; upper track) vs. COSMIC signatures (v3; $n = 67$; lower track), per mNEN. mNEN are sorted based on unsupervised clustering (Ward.D; Euclidean distance; distances plotted in \log_{10} -scale) of the relative contribution of the nine de novo mutational signatures.

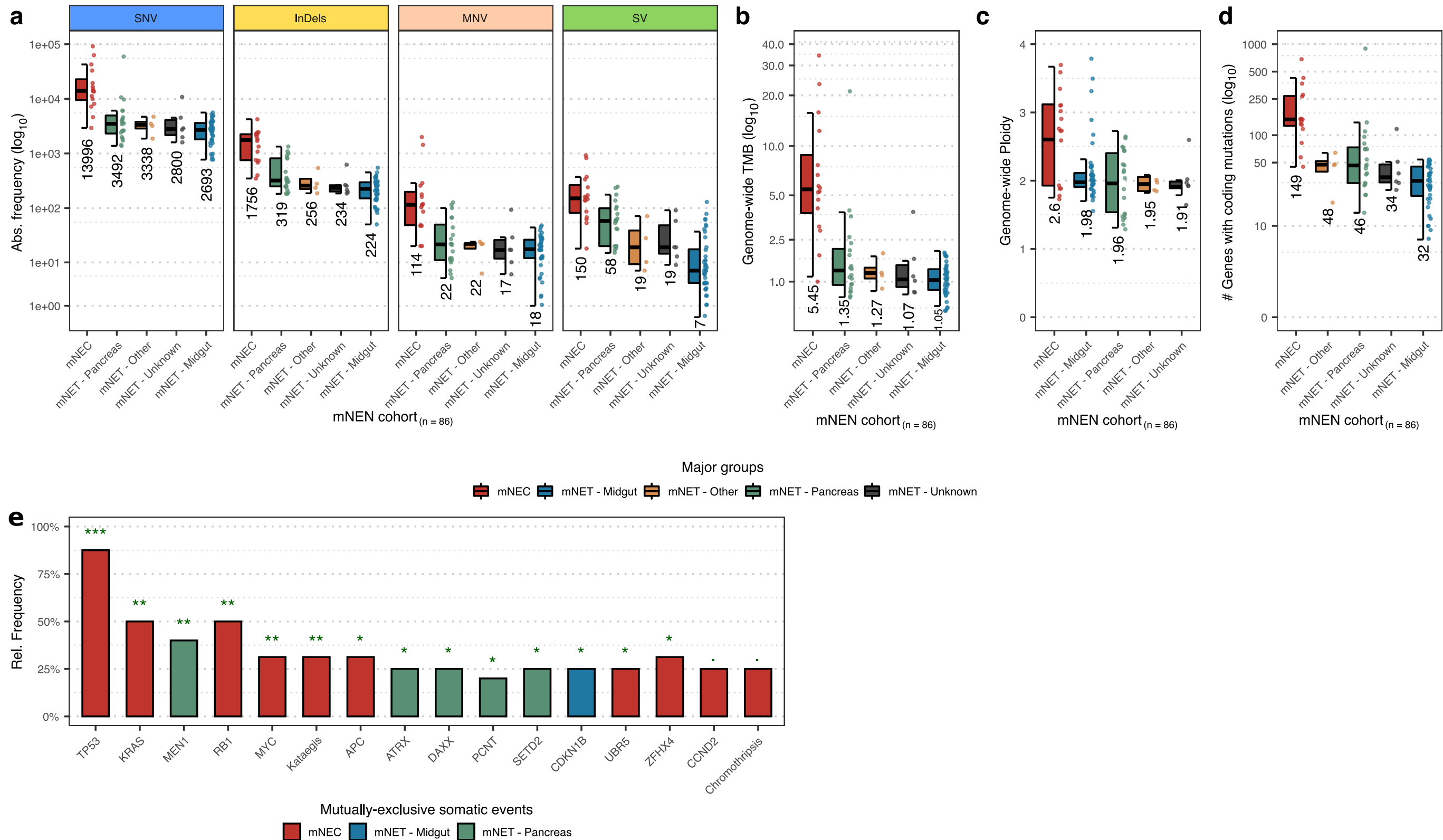
b) Cosine similarity of the de novo mutational signatures against the known COSMIC v3 signatures ($n = 67$).

c) Trinucleotide mutational contexts of the nine extracted de novo signatures.

d) NMF quality metrics using between two to fifteen ranks over 1000 iterations.



Supp. Figure 8 - Copy-number overview of mNEN cohort and subpopulations with re-occurring and focal amplifications and deletion highlighted (GISTIC2) and unbiased driver gene analysis. Circosplots with ideogram of recurrent copy-number aberrations as detected by GISTIC2 per sub-population (as shown above each circosplot). G-scores are depicted on the y-axis. Regions with amplifications (G-score > 0) are depicted in green and deletions (G-score < 0) in blue. Regions with significant (and recurring) copy-number aberrations ($q \leq 0.1$) are denoted with a darker shade of green or blue, respective of amplification or deletion. Per region, the foci of maximal amplification or deletion (focal peaks; $q \leq 0.1$) are denoted in the inner track; the peak identifiers with associated genes are also denoted and presented in supplementary table 1.



Supp. Figure 9 - Genomic characteristics per differentiation grade (NEC/NET) and primary localization within mNET.

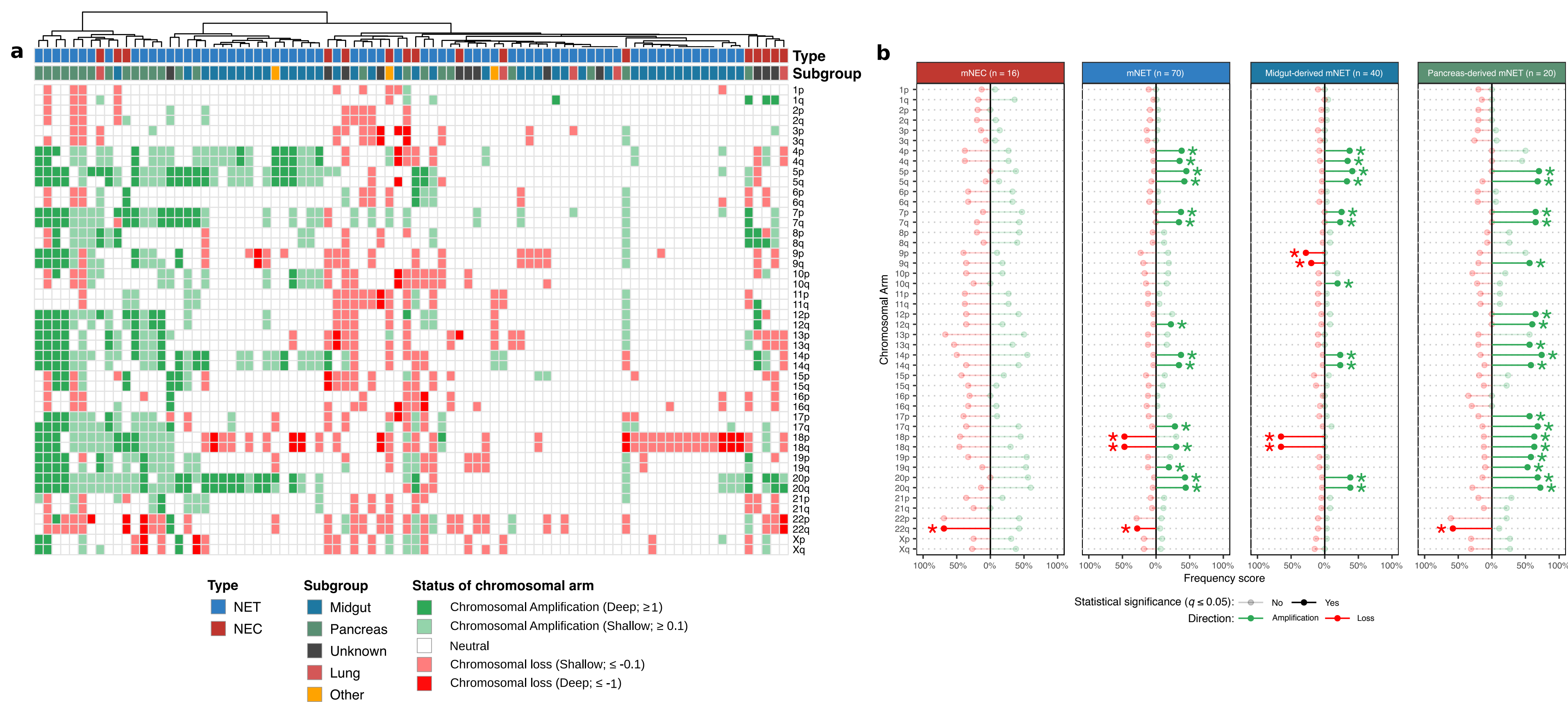
a) Number of SNV, InDels, MNV and SV per whole-genome mNEN with observed median per variable displayed. Data is categorized on mNEC and distinct mNET subgroups based on primary localization.

b) Tumor mutational burdens (genome-wide; \log_{10}), with observed median per variable displayed. Data is categorized on mNEC and distinct mNET subgroups based on primary localization.

c) Mean genome-wide ploidy, with observed median per variable displayed. Data is categorized on mNEC and distinct mNET subgroups based on primary localization.

d) Number of genes harboring somatic coding mutations, with observed median per variable displayed. Data is categorized on mNEC and distinct mNET subgroups based on primary localization.

e) Mutational enrichment of mutant genes (mutations and copy-number alterations) and large-scale events (kataegis and chromothripsis) between our three major subgroups; mNEC, pancreas- and midgut-derived mNET. Statistical significance was tested using a one-sided Fisher's Exact Test with BH correction; significance is denoted by *** ($q \leq 0.001$), ** ($q \leq 0.01$), * ($q \leq 0.05$) and . ($q \leq 0.1$).



Supp. Figure 10 - Copy-number aberrations of chromosomal arms per differentiation grade (NEC/NET) and primary localization within mNET.

a Unsupervised clustering (Euclidean distances, Ward.D2 method) of the mNET samples based on the categorization of chromosomal arm copy-number aberrations (based on GISTIC2 value per arm). Top color-bars depict the differentiation grade of the mNET (mNEC in red, mNET in blue) and the primary localization.

b Overview of the relative frequency of samples with amplifications (green) and losses (red) per arm within the given subgroup. Statistically significant ($q \leq 0.05$) arm-level copy-number aberrations are depicted with an asterisk whilst the non-significant events are shown as transparent.

Figures

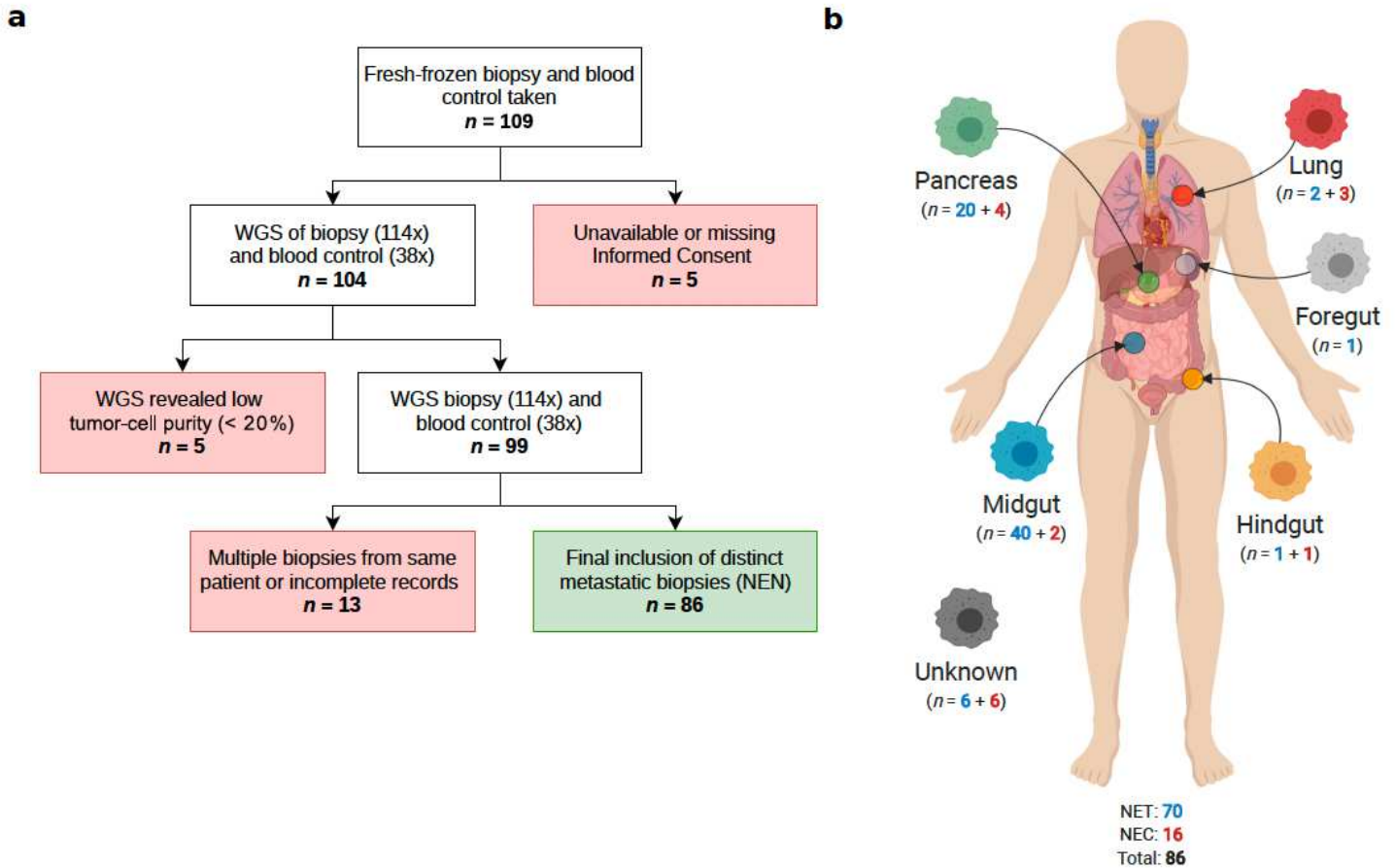


Figure 1

Overview of patient inclusion and sub-classification of biopsies. a) Flowchart of patient inclusion. From the CPCT-02 cohort, single biopsies from 86 distinct patients with metastatic neuroendocrine neoplasms (mNEN) were selected. From the total pool of available whole-genome sequenced mNET samples. If multiple derived mNET biopsies from the same patient were available, we selected the mNET biopsy with the highest tumor cell purity. b) Subclassification of mNEN based on primary localization. The 86 mNEN were subclassified, based on their primary localization, into six major categories; Foregut, Hindgut, Lung, Pancreas and Midgut; whilst samples with indeterminable localization were categorized as Unknown. The number of mNET (in blue) and mNEC (in red) are shown per category.

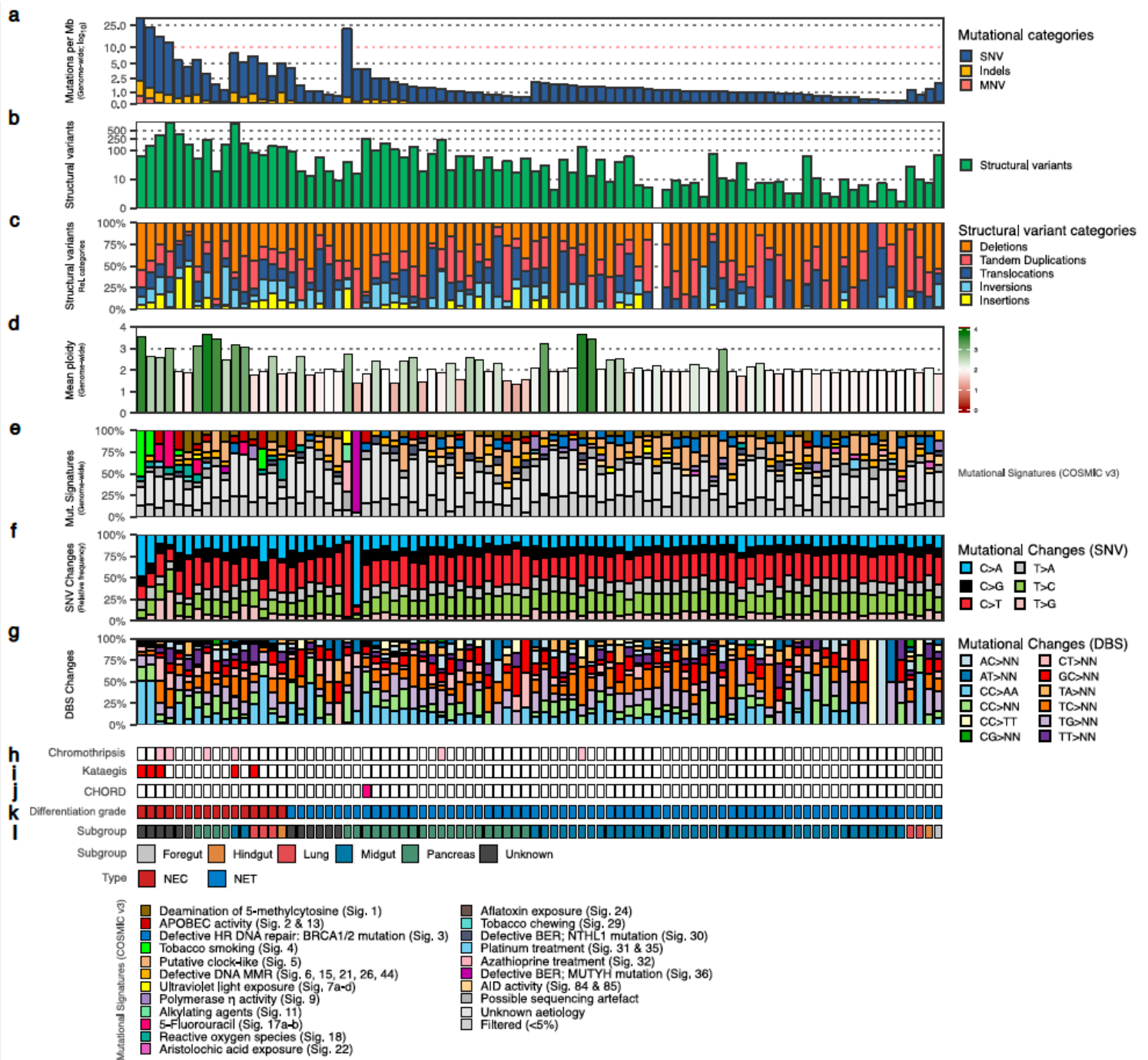


Figure 2

Landscape of large-scale genomic alterations detected in mNEN, ordered by differentiation grade (NEC / NEC) and primary localization. Overview of genome-wide characteristics of the mNEN cohort ordered by mNEC / mNET and primary localization on decreasing median tumor mutational burden. For each mNEN ($n = 86$), the following tracks are shown: a) Number of genomic mutations per megabase over the entire genome (TMB); SNV, InDel and MNV are depicted in blue, orange and salmon respectively. Threshold for high-TMB (≥ 10) is shown by a horizontal red dotted line. Y-axis is shown in log₁₀- scale. b) Total number of structural variants including deletions, tandem duplications, translocations, inversions and insertions as detected by GRIDSS. Y-axis is shown in log₁₀-scale. c) Relative frequency of each of the structural

variant categories; deletions in orange, tandem duplications in red, translocations in blue, inversions in light-blue and insertions in yellow. d) Mean genome-wide ploidy, ranging from 0 (red) to 4 (green; tetraploid). Common diploid status is shown in white. e) Relative contribution of the COSMIC single-base substitution mutational signatures (v3; n = 67). Signatures with less than 5 percent overall contribution within the entire mNEN cohort were categorized under the "Filtered (<5%)" category. The proposed etiology of the signatures is denoted below. f) Relative frequency of the pyrimidine mutations (SNV) in their six categories. g) Relative frequency of Doublet Base Substitution (DBS) categories. h) Presence of chromothripsis; mNEN with chromothripsis are shown in pink. i) Presence of kataegis; mNEN with kataegis are shown in red. j) Status of homologous recombination deficiency (HRD), as determined by CHORD; mNEN with BRCA1/2-associated HRD ($p \geq 0.5$) are shown in pink., otherwise colored white. k) Differentiation grade of the mNEN; NEC in red, NET in blue. l) Primary localization of the mNEN.

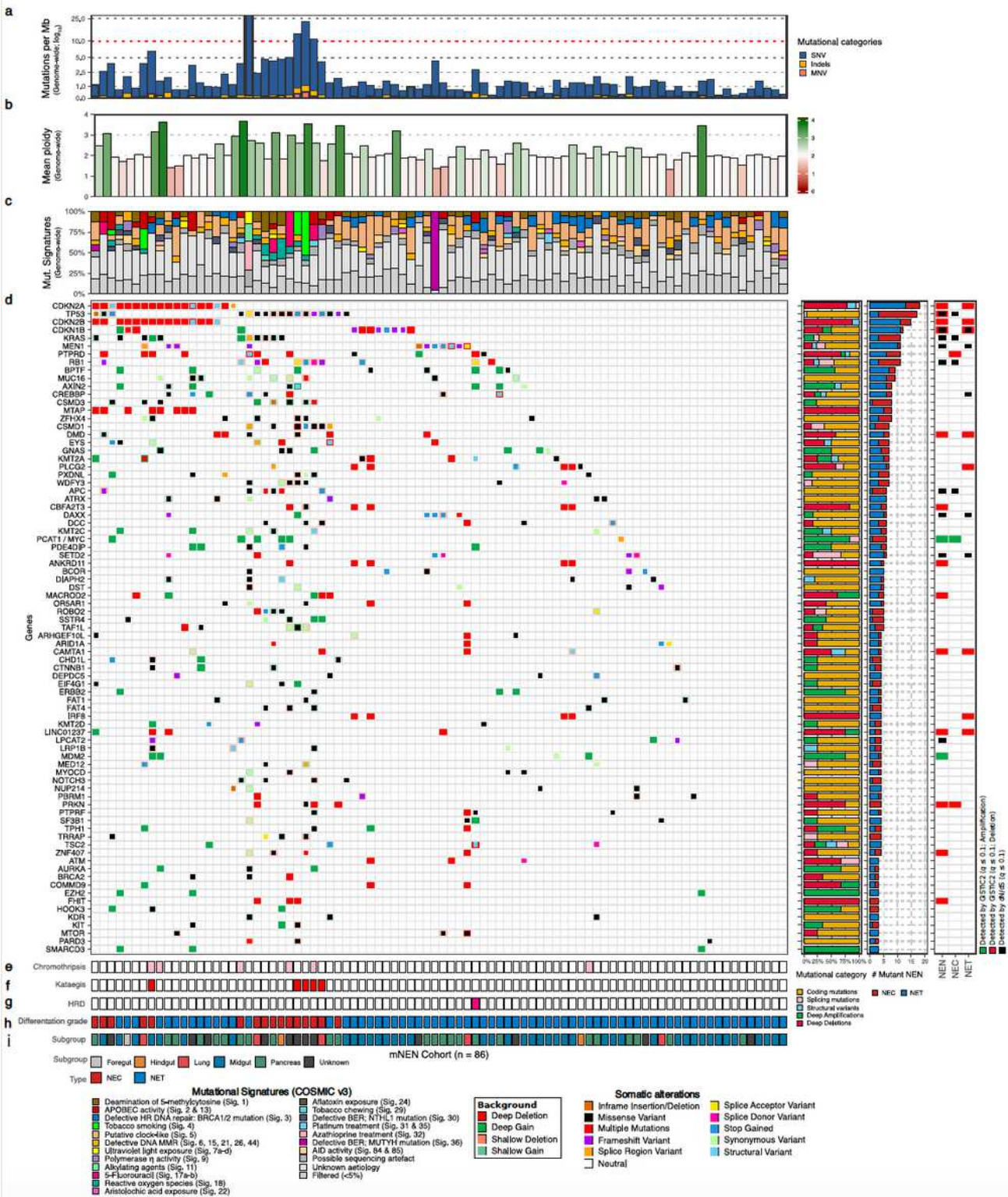


Figure 3

Putative drivers and NEN-associated genes within the mNEN cohort as detected by unbiased discovery (dN/dS, GISTIC2) and literature. Overview of putative drivers harboring coding mutations within at least three mNEN. We show putative drivers as detected by dN/dS and/or GISTIC2 and supplemented this list with additional NEN-associated drivers. mNEN and genes are sorted based on mutually exclusivity of the depicted putative drivers. Only GISTIC2 focal peaks with deep amplifications and deletions are shown. a)

Number of genomic mutations per megabase over the entire genome (TMB); SNV, InDel and MNV are depicted in blue, orange and salmon respectively. Threshold for high-TMB (≥ 10) is shown by a horizontal salmon dashed line. Y-axis is shown in log₁₀- scale. b) Mean genome-wide ploidy, ranging from 0 (red) to 4 (green; tetraploid). Diploidy is shown in white. c) Relative contribution of the COSMIC single-base substitution mutational signatures (v3; n = 67). Signatures with less than 5 percent overall contribution within the entire mNEN cohort were categorized under the "Filtered (<5%)" category. The proposed etiology of the signatures is denoted below. d) Overview of coding mutation(s) per mNEN, (light-)green or (light-)red backgrounds depict copy-number aberrations whilst the inner square depicts the type of (coding) mutation(s). The adjacent bar plots represent the relative proportions of mutational categories (coding mutations (SNV, InDels and MNV), splicing mutations, SV, deep gains (high-level amplifications resulting in many additional copies) and deep deletions (high-level losses resulting in (near) homozygous losses) per gene. The middle-outer barplot depicts the percentage of mNEC (in red) and mNET in blue which harbored a mutation. In addition, dN/dS and/or GISTIC2 support are shown on the outer-right bar plots for either the entire mNEN cohort or separate mNET/mNEC analysis; GISTIC2 results are colored red if these genes were detected within a recurrent focal deletion and green if detected within a recurrent focal gain. e) Presence of chromothripsis; mNEN with chromothripsis are shown in pink. f) Presence of kataegis; mNEN with kataegis are shown in red. g) Status of homologous recombination deficiency (HRD), as determined by CHORD; mNEN with BRCA1/2-associated HRD ($p \geq 0.5$) are shown in pink., otherwise colored white. h) Differentiation grade of the mNEN; mNEC in red, mNET in blue. i) Primary localization of the mNEN.

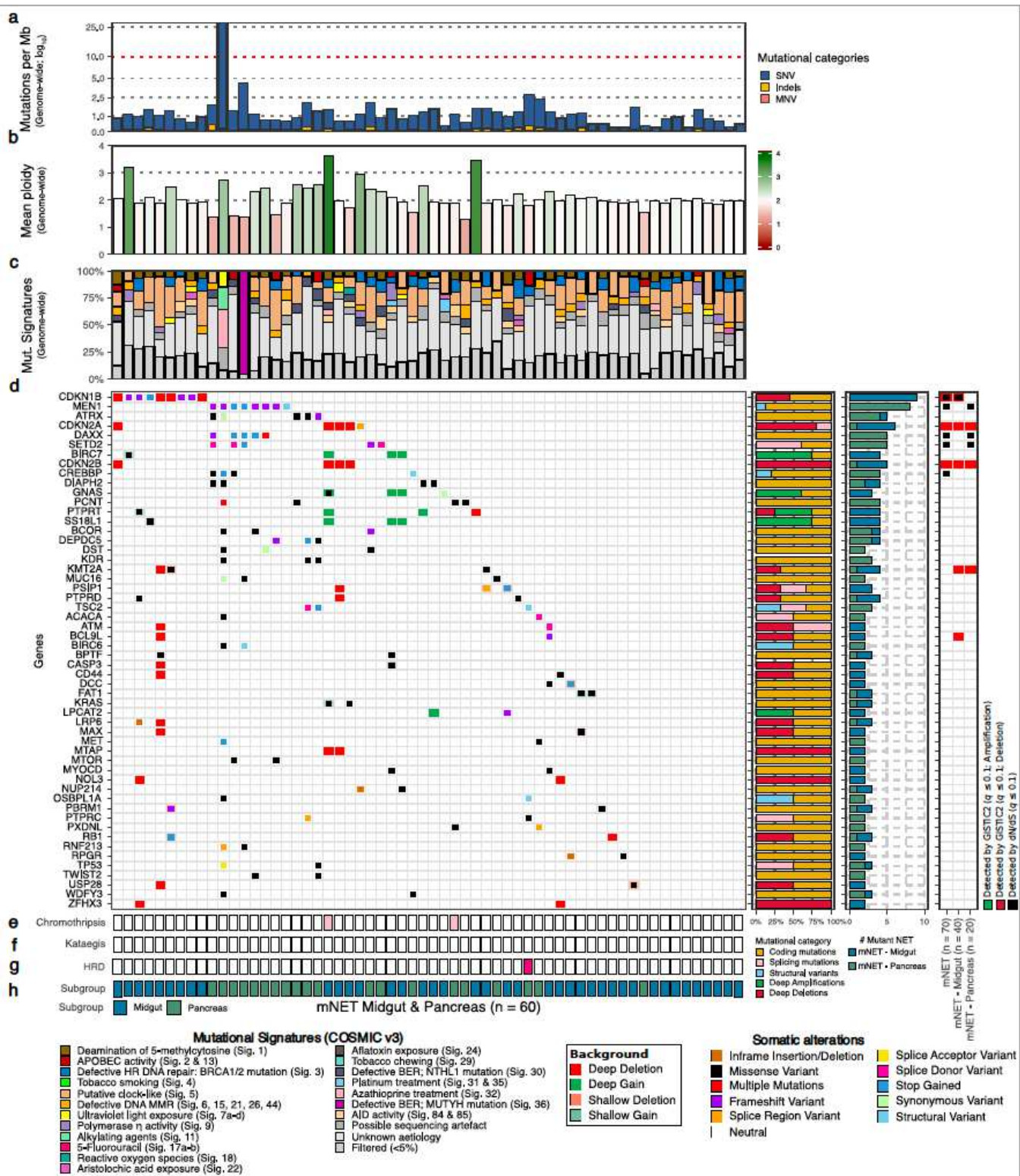


Figure 4

Putative drivers and NEN-associated genes within the pancreas- and midgut-derived mNET as detected by unbiased discovery (dN/dS, GISTIC2) and literature. Overview of putative drivers harboring coding mutations within at least two pancreasand/ or midgut-derived mNET. We show putative drivers as detected by subgroup-specific dN/dS and/or GISTIC2 and supplemented this list with additional NEN-associated drivers. mNET and genes are sorted based on mutually-exclusivity of the depicted putative

